

AD-A128 431

ATMOSPHERIC EFFECTS IN SATELLITE IMAGING OF MOUNTAINOUS TERRAIN(U) MASSACHUSETTS INST OF TECH CAMBRIDGE
ARTIFICIAL INTELLIGENCE LAB R W SJOBERG SEP 82

1/1

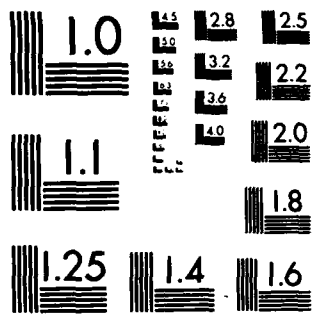
UNCLASSIFIED

AI-TR-688 N00014-80-C-0505

F/G 22/2

NL

END
DATE
FILED
6-83
DTIC



MICROCOPY RESOLUTION TEST CHART
NATIONAL BUREAU OF STANDARDS-1963-A

AD A 198431

UNCLASSIFIED

SECURITY CLASSIFICATION OF THIS PAGE (When Data Entered)

REPORT DOCUMENTATION PAGE		READ INSTRUCTIONS BEFORE COMPLETING FORM
1. REPORT NUMBER Technical Report 688	2. GOVT ACCESSION NO. AD-A128431	3. RECIPIENT'S CATALOG NUMBER
4. TITLE (and Subtitle) Atmospheric Effects in Satellite Imaging of Mountainous Terrain	5. TYPE OF REPORT & PERIOD COVERED MT	
	6. PERFORMING ORG. REPORT NUMBER	
7. AUTHOR(s) Robert W. Sjoberg	8. CONTRACT OR GRANT NUMBER(s)	
9. PERFORMING ORGANIZATION NAME AND ADDRESS Artificial Intelligence Laboratory 545 Technology Square Cambridge, Massachusetts 02139	10. PROGRAM ELEMENT, PROJECT, TASK AREA & WORK UNIT NUMBERS	
11. CONTROLLING OFFICE NAME AND ADDRESS Advanced Research Projects Agency 1400 Wilson Blvd Arlington, Virginia 22209	12. REPORT DATE September 1982	
	13. NUMBER OF PAGES pages 86	
14. MONITORING AGENCY NAME & ADDRESS (if different from Controlling Office) Office of Naval Research Information Systems Arlington, Virginia 22217	15. SECURITY CLASS. (of this report) UNCLASSIFIED	
	15a. DECLASSIFICATION/DOWNGRADING SCHEDULE	
16. DISTRIBUTION STATEMENT (of this Report) Distribution of this document is unlimited.		
17. DISTRIBUTION STATEMENT (of the abstract entered in Block 20, if different from Report)		
18. SUPPLEMENTARY NOTES None		
19. KEY WORDS (Continue on reverse side if necessary and identify by block number) image understanding satellite sensing remote sensing landsat atmospheric effects mountainous terrain digital terrain models hill-shading		
20. ABSTRACT (Continue on reverse side if necessary and identify by block number) >It is possible to obtain useful maps of surface albedo from remotely-sensed images by eliminating effects due to topography and the atmosphere, even when the atmospheric state is not known. A simple phenomenological model of earth radiance that depends on six empirically determined parameters is developed under certain simplifying assumptions. The model incorporates path radiance and illumination from sun and sky and their dependencies on surface altitude and orientation. It takes explicit account of surface shape, represented by a		

DD FORM 1473

1 JAN 73

EDITION OF 1 NOV 65 IS OBSOLETE
S/N 0102-014-6601

UNCLASSIFIED

SECURITY CLASSIFICATION OF THIS PAGE (When Data Entered)

digital terrain model, and is therefore especially suited for use in mountainous terrain. A number of ways of determining the model parameters are discussed, including the use of shadows to obtain path radiance and to estimate local albedo and sky irradiance. The emphasis is on extracting as much information from the image as possible, given a digital terrain model of the imaged area and a minimum of site-specific atmospheric data. The albedo image, introduced as a representation of surface reflectance, provides a useful tool to evaluate the simple imaging model. Criteria for the subjective evaluation of albedo images are established and illustrated for Landsat multispectral data of a mountainous region of Switzerland.

**ATMOSPHERIC EFFECTS IN SATELLITE
IMAGING OF MOUNTAINOUS TERRAIN**



Robert W. Sjoberg
Massachusetts Institute of Technology
Artificial Intelligence Laboratory
Cambridge, MA 02139

September, 1982

Accession For	
NTIS GRA&I	<input checked="" type="checkbox"/>
DTIC TAB	<input type="checkbox"/>
Unannounced	<input type="checkbox"/>
Justification	
By _____	
Distribution/	
Availability Codes	
Dist	Avail and/or Special
A	

Copyright © 1982 by Robert W. Sjoberg

This report is a revised version of a dissertation submitted May 22, 1981 to the Department of Electrical Engineering and Computer Science, M.I.T., in partial fulfillment of the requirements for the degree of Master of Science.

The research described herein was done at the Artificial Intelligence Support for the Laboratory's artificial intelligence research is provided in part by the Defense Advanced Research Projects Agency under Office of Naval Research contract N00014-80-C-0505.

Abstract

It is possible to obtain useful maps of surface albedo from remotely-sensed images by eliminating effects due to topography and the atmosphere, even when the atmospheric state is not known. A simple phenomenological model of earth radiance that depends on six empirically-determined parameters is developed under certain simplifying assumptions. The model incorporates path radiance and illumination from sun and sky and their dependencies on surface altitude and orientation. It takes explicit account of surface shape, represented by a digital terrain model, and is therefore especially suited for use in mountainous terrain. A number of ways of determining the model parameters are discussed, including the use of shadows to obtain path radiance and to estimate local albedo and sky irradiance. The emphasis is on extracting as much information from the image as possible, given a digital terrain model of the imaged area and a minimum of site-specific atmospheric data. The albedo image, introduced as a representation of surface reflectance, provides a useful tool to evaluate the simple imaging model. Criteria for the subjective evaluation of albedo images are established and illustrated for Landsat multispectral data of a mountainous region of Switzerland.

Acknowledgements

The author wishes to specially thank Prof. Berthold K. P. Horn for supervising the present research and for many useful discussions and encouragement. The financial and computational support provided by Prof. Patrick H. Winston and the Artificial Intelligence Laboratory are gratefully acknowledged. The author would also like to thank Dr. Kurt Brassel for providing the original digital terrain model of the Dent de Morcles and Les Diablerets regions, and Prof. Robert J. Woodham, now of the University of British Columbia, for timely comments and criticism.

Contents

1. Introduction	1
2. Derivation of the Sensor Radiance Model	5
2.1 Image-Forming Equation	5
2.2 Target Radiance	6
2.3 Transmission	7
2.4 Path Radiance	8
2.5 Model Assumptions	8
2.6 Sensor Radiance Equation	10
2.7 Exponential Forms	10
3. Determining Model Parameters	13
3.1 Description of the Test Area	13
3.2 Difficulties with Parameter Fitting	14
3.3 Information Sources External to the Image	15
3.3.1 Optical Depth	15
3.3.2 Path Radiance and Sky Irradiance	15
3.4 Information Sources Within the Image	16
3.4.1 Use of Calibration Targets	17
3.4.2 Using Shadows to Calibrate the Image	17
4. Generation of Albedo Images	21
4.1 Criteria for a Good Albedo Image	21
4.2 Model A	22
4.3 Model B	23
4.4 Model C	24
4.5 Qualitative Effects of Changing Model Parameters	25
5. Summary	27
6. Conclusions	31
7. References	33
Tables	37
Figures	42

Tables and Figures

Table 1. Orbital and multispectral scanner parameters for Landsat 1.	37
Table 2. Theoretical path radiance L_p values by optical depth.	38
Table 3. Theoretical sky irradiance on a horizontal surface.	39
Table 4. Measured atmospheric radiometric quantities.	40
Table 5. Model parameters used in models D1 through D12.	41
Figure 1. Global coordinate system	42
Figure 2. Local (target) coordinate system	44
Figure 3. Optical depth and vertical transmission <i>vs.</i> altitude	46
Figure 4. Atmospheric radiation components	48
Figure 5. Turner-Spencer <i>vs.</i> exponential path radiance	50
Figure 6. Turner-Spencer <i>vs.</i> exponential sky irradiance	52
Figure 7. Isometric plot of the Dent de Morcles region	54
Figure 8. Digital elevation model of the Dent de Morcles region	56
Figure 9. Landsat 1 multispectral scanner band 4 image	58
Figure 10. Binary maps of cast and self-shadows	60
Figure 11. Synthetic satellite image assuming no atmosphere	62
Figure 12. Optical depth <i>vs.</i> altitude for the reference atmosphere	64
Figure 13. Optical depth of the exponential models	66
Figure 14. Minimum sensor radiance altitude profile	68
Figure 15. Two possible exponential models of path radiance	70
Figure 16. Altitude profile of average albedo from sunlit targets	72
Figure 17. Comparison of exponential and linear path radiance models	74
Figure 18. Model A albedo image and its associated histogram.	76
Figure 19. Model B albedo image and its associated histogram.	78
Figure 20. Model C albedo image and its associated histogram.	80
Figure 21. Qualitative effects of varying model atmospheric parameters	82

PRECEDING PAGE BLANK-NOT FILMED

1. Introduction

The goal of multispectral remote sensing is to recover information about the imaged scene. This information is usually surface reflectance, an intrinsic property of the material comprising the surface and independent of the imaging situation particulars: illumination, topography, sensor position. Reliable recovery of reflectance demands an accurate model of the imaging process, embodied in what is called the *image-forming or image irradiance equation*. This equation describes image irradiance as a function of local surface reflectance, incident illumination, sensor optical properties, and other radiometric quantities that affect it. It is necessary to invert the equation in order to express reflectance as a function of image irradiance and other parameters and thereby compute the desired surface description.

Inverting the image-forming equation is a difficult task in high-altitude satellite sensing of the earth due to the presence of the atmosphere. The atmosphere affects satellite imaging in at least three ways that must be incorporated into the imaging equation: it attenuates energy passing through, it confounds the desired signal with irrelevant or spurious radiance, and it imposes a distributed surface illuminant in the form of sky irradiance. A substantial literature has developed on the relationship of atmospheric optics to remote sensing. A sample of that literature can be found in the extensive bibliography of Howard and Garing [1]. The reader is referred to McCartney's [2] book on atmospheric optics and Rozenberg's [3] treatise on light scattering for introductory material. LaRocca and Turner [4] have recently published a comprehensive state-of-the-art review of methods for computing atmospheric quantities applicable to remote sensing.

The interaction of atmospheric effects with those of topography makes it difficult to study remote sensing in mountainous terrain, but such regions are important. Earth-sensing satellites are widely used to help map natural resources, a very large fraction of which are concentrated in mountainous terrain. Such areas are often inaccessible to direct survey methods, and one must rely on remote sensing to provide needed information. Without an understanding of how rugged topography, atmosphere, and the surface interact in an imaging situation, it is impossible to develop computational schemes to help automate the interpretation process. There are not sufficient skilled photogrammetrists to begin to handle the quantity of satellite data made possible through such programs as Landsat.

Despite the importance of acquiring information about such areas, there have been relatively few successful applications of remotely-sensed images to mountainous terrain. Among the earliest reported were photometric studies of Mars. Path radiance was estimated from image brightness by subtracting some value due to reflection of sunlight. From this, air column depth and subsequently altitudes could be computed [5]. Another study used brightness variations to estimate surface slope [6]. In studies of terrestrial scenes, Hoffer and his coworkers were among the first to at least recognize the role of cast shadows in images of rugged topography [7]. Explicit slope and elevation data have been used several

times as separate channels in the automated classification process [8,7,9]. Later studies have recognized the role of slope and elevation in the imaging process. Sadowsky and Malila [10] used slope information to account for foreshortening and self-shadow. A recent paper described field experiments and satellite simulations to explicitly study the "topographic effect" on remote imaging [11]. The simulations were, however, specifically designed to minimize and ignore atmospheric interactions by assuming clear sky conditions and focussing on spectral channels in which the atmospheric effects are not normally significant.

The motivation for the approach taken in the present research stems from successful work with synthetic images in the field of machine vision. Horn's computational attack on recovering three-dimensional shape from shading information in a monocular image lead directly to the development of the reflectance map to represent the dependence of reflected radiance on surface orientation [12]. The reflectance map was developed and successfully applied to other problems in shape extraction [13,14,15] and photometric stereo [16,17,18]. The reflectance map was also valuable in investigating reverse shape-from-shading problems. Here, surface shape and composition are assumed, and reflectance map techniques are applied to produce a synthetic image of the surface under stated illumination conditions. Digital terrain models provided convenient surface descriptions for use in the study of hill-shading for maps [19], and in the automatic registration of satellite images with surface models [20]. More recent work on the use of digital terrain models to model image formation in remote sensing (including atmospheric and topographic effects) has been reported by Woodham [21].

The three goals of the research presented in this paper were (1) to develop a simple model of the image-forming equation suitable when viewing rough terrain through an atmosphere; (2) to explore ways of determining the model parameters directly from a satellite image; and (3) to present the albedo map as a representation of surface reflectance and to evaluate it as a tool in determining model parameters.

An albedo image or albedo map is a synthetic image that captures surface reflectance under the assumption of a Lambertian earth. It thus represents an intrinsic property of the terrain cover, and is invariant with respect to terrain shape, sun and sensor position, and atmospheric state. Several such images from different spectral channels can be combined to produce a false-color map of terrain cover. Or, the composite albedo data may be fed to a pattern classification system. Since the albedo map more closely represents surface properties than the raw image, better classification results are expected.

An albedo map can be generated only after the image-forming equation has been inverted, expressing local albedo in terms of topographic, atmospheric, and sensor optical effects. Effects due to the sensor itself are presumably known. Those due to topography can be determined from a suitable digital terrain model of the area imaged. Atmospheric effects, on the other hand, are not easily determined. A complete treatment involves the solution of the three-dimensional, non-linear, integro-differential radiative transfer equation appropriate to a spherical earth

[4,22,23,24]. This is computationally infeasible, even if the required information were available.

By adopting a number of general assumptions, the image-forming equation is greatly simplified as will be shown. The most important assumptions are:

1. the atmosphere is a horizontally homogeneous medium;
2. the earth is a Lambertian reflector with pointwise-varying albedo;
3. skylight is approximately uniform across the sky;
4. atmospheric radiometric quantities vary exponentially with altitude.

The result is a six-parameter model of the imaging process, where the parameters are empirically determined from the image and auxiliary data. Without site-specific information, however, it is difficult to obtain trustworthy values.

A trial-and-error approach is advocated. An albedo image is generated using a trial set of model parameters, and evaluated according to subjective criteria of its acceptability. Adjustments are made in the values of the parameters, another albedo image is produced, and the evaluation is repeated. Although no formalism for determining an optimal albedo image is given, limited experience with the method indicates that satisfactory results can be obtained.

The procedure outlined has been useful in illustrating the nature of the interactions of topography and the atmosphere in satellite sensing. One finds that the direct solar irradiance dominates over most of the sunlit image. However, surface elements at near-grazing incidence or in shadow are especially sensitive to variations in sky irradiance. Path radiance is probably the single most important contribution to the sensed signal over the entire image, in that the computation of albedo is most sensitive to it. Fortunately, the presence of shadows in the scene actually helps to determine the path radiance. Sky irradiance and other parameters are not so easy to find from the image due to noise in both the image and in the digital terrain model. But the trial-and-error approach using albedo maps nonetheless allows one to obtain a reasonably good description of surface cover. Finally, it is emphasized that planners of future satellite observation systems would do well to incorporate auxiliary sensors on-board to help determine the necessary atmospheric quantities.

2. Derivation of the Sensor Radiance Model

The image-forming equation relates the distribution of irradiance across the sensitive surface of an imaging device to the radiance of the scene viewed. Woodham [13] identifies four factors that interact in an imaging situation:

1. the geometry of the source, viewer, and scene;
2. the spatial and spectral distribution of illumination;
3. the photometric properties of the viewed surfaces;
4. the topography of the viewed object, its shape.

In most situations, image irradiance is directly proportional to scene radiance [25]. In high-altitude optical sensing of the earth, however, one must reckon with the presence of the transmitting medium, the atmosphere. The atmosphere attenuates light reaching the surface and reflected from it. It further imposes a distributed surface illuminant in the form of skylight. In this case, image irradiance is proportional to the sum of the attenuated radiance of the imaged surface and the atmospheric or path radiance. All five interactions--the four above plus the atmosphere--must be suitably modeled before the image-forming equation can be inverted to obtain surface reflectance.

Although the atmosphere affects all remote sensing situations to some degree, the effects become particularly important when viewing areas of rugged topography. One effect is due to varying elevation across the scene. The air mass between the sensor and the surface diminishes with altitude, and atmospheric effects are consequently reduced. There is less attenuation of solar illumination and reflected radiance, less skylight, and less extraneous path radiance at higher altitude. Another effect is due to wide variation in surface orientation across the scene. The slope of a surface element determines its exposure to sunlight and skylight. An element that slopes away from the sun sufficiently is self-shadowed and receives no sunlight. Even surfaces that would otherwise be sunlit may lie in shadows cast by surrounding terrain features. Shadows are abundant in Landsat images of mountainous regions because of the early morning overflight time. By modeling the contribution of skylight to the reflected surface radiance, it is possible to recover information about the ground even in shadows.

2.1. Image-Forming Equation

The signal generated by a remote imaging system depends on the irradiance striking the photosensitive surface of the sensor. We shall assume that the characteristics of the optical system are sufficiently determined that one can recover this irradiance from the signal by inverting the sensor's transfer function. For a small aperture, the sensor irradiance is approximately the product of the directional irradiance [26] and the solid angle subtended by the aperture, $\Delta\omega$. The directional irradiance is the sum of the attenuated radiance of the surface and atmospheric path radiance. Thus the image-forming equation is

$$E_i(x_i, y_i) = [L_t(r_t, r_m)T_u(r_t, r_m) + L_p(r_t, r_m)]\Delta\omega \quad (1)$$

where

- $E_i(x_i, y_i)$ = the sensor irradiance at image coordinates (x_i, y_i) ;
 $L_t(r_t, r_m)$ = the radiance from the target in the direction of the sensor;
 $T_u(r_t, r_m)$ = the atmospheric transmission of radiance from the target to the sensor;
 $L_p(r_t, r_m)$ = the atmospheric radiance introduced in the path between the target and the sensor.
 r_t = the position of the imaged surface element (called "target" below) in a global coordinate system;
 r_m = the position of the sensor in the global coordinate system;

Although one necessarily works with the sensor signal, from which image irradiance can be computed, the subsequent discussion is more concerned with the radiances that comprise the directional irradiance. The term "sensor radiance" will be used below to denote this directional irradiance:

$$L_m(r_t, r_m) = L_t(r_t, r_m)T_u(r_t, r_m) + L_p(r_t, r_m) \quad (2)$$

The image-forming equation given here is time- and wavelength-independent. It is assumed that all radiometric quantities refer to spectral averages over the wavelength interval of interest and that the time to capture an image is short enough that there are no fluctuations of the quantities involved.

It is convenient to establish a global Cartesian coordinate system. This is appropriate for satellite images as used here, provided some rectification is applied to the image to compensate for earth curvature. The global z -axis is taken to be radially outward, and the x -axis to point directly east (figure 1). Directions in this system are specified as pairs of polar coordinates (θ, ϕ) . The sun and satellite have direction (θ_0, ϕ_0) and (θ_m, ϕ_m) respectively in this system.

2.2. Target Radiance

The target radiance $L_t(r_t, r_m)$ depends on the photometric properties of the surface and the distribution of the illumination. Surface photometry is described by the bidirectional reflectance-distribution function (BRDF), $f_r(r_t; \theta_i, \phi_i; \theta_r, \phi_r)$, where (θ_i, ϕ_i) and (θ_r, ϕ_r) specify the angles of energy incidence and emittance, respectively [26]. These directions are given in a polar coordinate system local to each target. The target's surface normal, pointing in direction (θ_n, ϕ_n) in the global reference frame, defines the z' -axis (figure 2). The x' -axis is arbitrarily chosen as the vertical projection of the x -axis onto the plane of the target. Using primes to indicate coordinates reckoned in the local system, the radiance reflected by the target toward the satellite sensor is

$$L_t(r_t, r_m) = \int_0^{2\pi} \int_0^{\pi/2} f_r(r_t; \theta'_i, \phi'_i; \theta'_n, \phi'_n) L_i(r_t; \theta_i, \phi_i) \cos \theta'_i \sin \theta'_i d\theta'_i d\phi'_i \quad (3)$$

(θ'_m, ϕ'_m) is the direction to the satellite in the local system and depends on \mathbf{r}_m . $L_i(\mathbf{r}_t; \theta_i, \phi_i)$ is the surface illumination at the target. The $\cos \theta'_i$ factor accounts for the foreshortening of the target area presented to the illuminant as the incident angle increases. The integral is over the hemisphere of directions to which the target is exposed.

One can transform the equation for target radiance into an integral over directions in the global coordinate system using the following transformation equations [25]:

$$\begin{aligned}\cos \theta &= \cos \theta_n \cos \theta' + \sin \theta_n \sin \theta' \cos(\phi_n - \phi') \\ \sin \theta \sin(\phi_n - \phi) &= \sin \theta' \sin(\phi' - \phi_n) \\ \sin \theta \cos(\phi_n - \phi) &= \sin \theta_n \cos \theta' - \cos \theta_n \sin \theta' \cos(\phi' - \phi_n)\end{aligned}\quad (4)$$

The primed quantities are coordinates in the local system; unprimed quantities are their counterparts in the global system. Interchanging the primed and unprimed quantities obtains the transformation from global coordinates into local coordinates.

The illumination function L_i (written as radiance although it is technically directional irradiance [26]) is a complex combination of attenuated solar irradiance, diffuse cloud and sky irradiance, and reflected ground radiance. Some of these components may be missing due to shadowing. Certain assumptions made below will simplify the target illuminant by neglecting all but two components.

2.3. Transmission

The reflected radiance is attenuated by its passage from the target at \mathbf{r}_t to the satellite at \mathbf{r}_m according to the factor $T_u(\mathbf{r}_t, \mathbf{r}_m)$. The transmission is simple to express as a function of optical thickness τ , which is a measure of the extinction properties (scattering and absorption) of the light path. The optical thickness of a path parameterized by s is $\tau(s) = \int_0^s \beta(s) ds$, where $\beta(s)$ is the volume extinction coefficient [2]. In the special case of a vertical transmission path from altitude z to an infinitely distant observer, the optical thickness of the atmosphere is called the optical depth:

$$\tau(z) = \int_z^\infty \beta(z) dz \quad (5)$$

By definition, the transmission of a light beam over a path of optical thickness τ is $T = e^{-\tau}$. Since $\tau \geq 0$, the transmission is bounded: $0 \leq T \leq 1$. For a distant sensor directly over the viewed earth scene, the upward transmission is

$$T_u(\mathbf{r}_t, \mathbf{r}_m) = e^{-\tau(z)} \quad (6)$$

where z is the altitude of the target at \mathbf{r}_t . Figure 3 displays both optical depth and vertical transmission for typical values.

Attenuation also affects the incident solar beam. If the sun is at position \mathbf{r}_0 in global coordinates and the incident extraterrestrial solar irradiance is E_0 , then a target oriented normal to the solar beam receives an irradiance

$$E_{sun}(\mathbf{r}_t) = E_0 T_d(\mathbf{r}_t) = E_0 \exp(-\tau(\mathbf{r}_0, \mathbf{r}_t)) \quad (7)$$

where $\tau(r_0, r_t)$ is the optical thickness of the path from the sun to the target. If the direction to the sun makes an angle θ_0 with respect to the global vertical (z -axis), then in the special case of a horizontally homogeneous atmosphere the transmission of the solar slant path is

$$T_d(r_t) = e^{-\tau(z)/\cos\theta_0} \quad (8)$$

where $\tau(z)$ is the optical depth of the target.

2.4. Path Radiance

The path radiance $I_p(r_t, r_m)$ includes light from outside the target that is scattered into the sensor path so as to appear to be from the target. Such atmospheric radiance comes from light reflected from the ground outside the target (the background), from a portion of the solar beam passing through the target-sensor path, and from multiply-scattered skylight. The path radiance does not include light from clouds that obscure part of the scene, which is better handled as a modification to the scene rather than a property of the light path. Path radiance must be modeled carefully, since it is a major contribution to the total radiance, and the recovery of surface albedo is very sensitive to it.

Figure 4 illustrates major contributions to the total radiance reaching the satellite sensor. A full account of each is given in the comprehensive review of LaRocca and Turner [4].

2.5. Model Assumptions

For the derivation of a fairly simple image-forming equation applicable in mountainous terrain, some basic assumptions reduce the number of relevant components to three, which depend on only six parameters.

A major assumption is that radiation in the atmosphere behaves as if the medium were an optically thin, semi-infinite, plane-parallel, horizontally homogeneous air mass. Variations occur only in the z -direction, reducing an inherently three-dimensional problem to one-dimensional. Specific contributions to the radiative behavior due to multiple scattering and absorption are ignored. These effects can be large in certain spectral regions in hazy atmospheres [27]. By adopting a phenomenological model based on empirically determined parameters, the major influences of these effects are incorporated as part of the aggregate behavior. The problem is reduced in some sense to its single-scattering equivalent.

A second fundamental assumption specifies that the earth surface is a Lambertian reflector, where the albedo is allowed to vary from point to point. The radiance of a Lambertian surface is independent of the angle of observation and depends only on the total irradiance and the surface albedo or bihemispherical reflectance ρ [26]. The BRDF in this case is

$$f_r(r_t; \theta_i, \phi_i; \theta_m, \phi_m) = \frac{\rho(r_t)}{\pi} \quad (9)$$

Such a model of earth reflectance has been popular in many investigations, even though its applicability has been seriously questioned [28]. The reflectance of most of the earth's surface that has been measured shows strong anisotropy, especially at low sun elevations [29]. However, the ground cover is generally not known *a priori*; indeed that is one goal of analyzing remotely sensed images. With no other information on the geometric reflectance properties of the viewed scene, it is necessary to assume something, and a Lambertian surface is mathematically convenient. There is still the problem of determining the local albedo.

The third major assumption is that of a uniform hemispherical sky. That is, no matter what the form of actual sky radiance, it is assumed here that it can be replaced by an equivalent uniform sky. Although not an accurate model of sky radiance as even the casual observer can verify, it is expedient to developing a simple model. The utility of this assumption is readily apparent when considering mountainous terrain. A non-horizontal surface element sees only a portion of the sky depending on its slope. The target irradiance integral eq. (3), even for a Lambertian surface, becomes extremely complex for sky radiance distributions that approach the forms given, for example, by Turner and Spencer [30] or by Otterman [31]. The integral can be evaluated for a uniform sky [32,25]:

$$E_{sky}(r_t) = E_s(z)h(\theta_n, \phi_n) = E_s(z)\frac{1}{2}(1 + \cos \theta_n) \quad (10)$$

where $E_s(z)$ is the sky irradiance on a horizontal surface at elevation z , and $h(\theta_n, \phi_n) = \frac{1}{2}(1 + \cos \theta_n)$ is the factor by which this irradiance is diminished for a surface whose normal makes an angle θ_n with the zenith.

The three assumptions above are essential to develop the simple model sought here. Other minor assumptions are also made to ease the computation. Both the sun and the satellite sensor are presumed to be geometric points infinitely distant. The sensor is assumed to be directly over the target scene to permit use of an orthographic projection.

Another convenient fiction is that the sensor has been perfectly calibrated and its response characteristics are known. Such an assumption is necessary for the inversion of the image-forming equation to determine albedo as a function of the sensor signal. Experience has shown that while the sensors for the Landsat series of satellites operate in close accord with their nominal radiometric parameters, the transformations performed on the raw sensor data to achieve this accord are inaccurate [33].

It is also assumed that errors in surface elevation and slope data are negligible. It was discovered after the digital elevation model for the test region had been obtained that in fact there were substantial errors introduced during the transcription process (the model was derived by manually tracing contour maps). These errors were magnified during the generation of the slope model by discrete differences. They appear most readily among ridges and valleys, but did not substantially degrade the performance of the albedo computation.

2.6. Sensor Radiance Equation

Under the conditions and assumptions stated above, the image-forming equation (1) becomes

$$L_m(x_t, y_t) = \frac{\rho(x_t, y_t)}{\pi} T_u(z) [E_0 T_d(z) R(\theta_n, \phi_n) + E_s(z) h(\theta_n, \phi_n)] + L_p(z) \quad (11)$$

where

$L_m(x_t, y_t)$ = the sensor radiance associated with the target at (x_t, y_t) ;

$\rho(x_t, y_t)$ = the albedo of the target at (x_t, y_t) ;

$T_u(z)$ = the vertical transmission from altitude z up to the sensor;

E_0 = the extraterrestrial solar irradiance on a normally-oriented surface;

$T_d(z)$ = the slant-path transmission from sun to altitude z ;

$R(\theta_n, \phi_n)$ = a function that captures the geometric dependence of reflectance as well as shadow information;

$E_s(z)$ = the sky irradiance on a horizontal surface at altitude z ;

$h(\theta_n, \phi_n)$ = the geometric dependence of sky irradiance on surface orientation as computed above;

$L_p(z)$ = the path radiance between the sensor and the surface at altitude z .

Altitude is obtained from the digital elevation model, $z = z(x_t, y_t)$, and slope and aspect from the digital slope model, $\theta_n = \theta_n(x_t, y_t)$ and $\phi_n = \phi_n(x_t, y_t)$. The function $R(\theta_n, \phi_n)$ describes the foreshortening of the surface as seen by the sun, and is zero if the target is shadowed:

$$R(\theta_n, \phi_n) = \begin{cases} 0, & \text{if target is self- or cast-shadowed} \\ \cos \theta'_0, & \text{if } 0 \leq \theta'_0 \leq \pi/2 \end{cases} \quad (12)$$

where θ'_0 is the zenith angle to the sun in local coordinates. It is the angle between the direction of the surface normal (θ_n, ϕ_n) and the solar direction (θ_0, ϕ_0) :

$$\cos \theta'_0 = \cos \theta_n \cos \theta_0 + \sin \theta_n \sin \theta_0 \cos(\phi_n - \phi_0)$$

This model is very simple and is easily inverted to obtain albedo, the only quantity depending explicitly on the target's (x, y) position:

$$\rho(x_t, y_t) = \frac{\pi [L_m(x_t, y_t) - L_p(z)]}{T_u(z) [E_0 T_d(z) R(\theta_n, \phi_n) + E_s(z) h(\theta_n, \phi_n)]} \quad (13)$$

In applying this model to a real image, the predicted radiance L_m is replaced by the recorded radiance L . The transmissions T_d and T_u have already been expressed in terms of optical depth (eqs. (6) and (8)).

2.7. Exponential Forms

The three unspecified atmospheric quantities--optical depth, sky irradiance, and path radiance--are taken to be independent exponential functions of altitude. In each case, the form is suggested by the observed behavior of the quantity in

question or theoretical calculations that predict such behavior. The exponential forms are good approximations to more complicated expressions, particularly for path radiance and sky irradiance, and they are easier to compute.

Optical depth is exactly exponential for an isothermal atmosphere, in which particle density decreases exponentially with altitude [2]. This does not hold generally for the earth's atmosphere, although large portions of it are nearly isothermal. A standard atmosphere has been adopted to facilitate research in atmospheric optics [34,35]. The U.S. Standard Atmosphere incorporates two distinct particle components, molecules and aerosols. Optical depth computed for either component separately behaves exponentially (see below), but this is not true of their sum.

Path radiance is exponential to a very good approximation, at least for lower terrestrial altitudes. This form is comparable to the established and respected model advanced by Turner and Spencer [30] and the more recent model of Otterman [31]. Figure 5 shows the Turner-Spencer model path radiance for a particular set of observation conditions.

Superimposed on this plot is an exponential curve whose two parameters (sea-level path radiance and scale height) were fitted to the computation data by least squares. The difference over the range of altitudes of interest in the present investigation is almost imperceptible. The agreement was considered sufficient justification for adopting an exponential form, where the parameters are to be determined.

The irradiance of the sky on a horizontal surface is also modeled as exponential with altitude. Comparison of the Turner-Spencer form of sky irradiance with the approximating exponential form again shows only a small difference (figure 6). It should be pointed out that because the sky is assumed here to be of uniform radiance, the angular and altitude dependencies are separable. The sky irradiance on a surface with a given tilt is a fixed fraction of that on a horizontal surface at the same altitude, and the fraction itself is independent of altitude. There are two parameters associated with horizontal sky irradiance, its sea-level value and a scale height, to be determined from the image data as described below.

No coupling is assumed to exist between the pairs of optical depth, path radiance, and sky irradiance parameters. Such coupling of course does exist explicitly in the radiative transfer formulation, which is being avoided here.

The three undetermined atmospheric radiometric quantities have the following forms:

$$\begin{aligned} \text{optical depth: } \tau(z) &= \tau_0 e^{-z/H} \\ \text{path irradiance: } L_p(z) &= L_{p0} e^{-z/H_p} \\ \text{sky radiance: } E_s(z) &= E_{s0} e^{-z/H_s} \end{aligned}$$

where the sky irradiance is on a horizontal target. The base constants τ_0 , E_{s0} , and L_{p0} and the scale factors H , H_s , and H_p are to be determined from the evaluation of synthetic albedo images as described below.

3. Determining Model Parameters

Before the simple satellite imaging model developed above can be used to generate albedo images, the parameters of the three atmospheric quantities must be determined. Since precise calibration data is generally not available to help determine the six unknowns—and this was particularly true for the site investigated here—it is necessary to assume values, or estimate them from the satellite image. These values can be used to generate a trial albedo image that can be inspected and judged by primarily subjective criteria. Adjustments to the parameters can be made and new albedo images created until satisfactory results are obtained.

3.1. Description of the Test Area

The region selected for the research lies in southwestern Switzerland, between $7^{\circ}1'$ and $7^{\circ}15'$ E and $46^{\circ}8'30''$ and $46^{\circ}21'5''$ N. The region, map titles *Dent de Morcles* and *Les Diablerets*, has been used in previous studies [20,36]. A digital elevation model (DEM) was obtained as an array of 174 by 239 values on a 100-meter grid, digitized from contour maps. The vertical quantization is 10 meters. Altitudes in the scene range from 410 meters in the valley of the Rhone River (southeast corner of the area) to 2310 meters on the Sommet des Diablerets (northeast corner). A model of local slopes was generated from the DEM by modified first differences [19], and stored as discrete coordinates in gradient space. Thus, the surface normal for each target in the scene was available as a discrete point $(p, q) = (\partial z/\partial x, \partial z/\partial y)$ in gradient space [12,13,19,37], from which its slope θ_n and aspect ϕ_n could be computed according to the transformation

$$\begin{aligned}\cos \theta_n &= \frac{1}{(1 + p^2 + q^2)^{1/2}} & \cos \phi_n &= \frac{-p}{(p^2 + q^2)^{1/2}} \\ \sin \theta_n &= \frac{(p^2 + q^2)^{1/2}}{(1 + p^2 + q^2)^{1/2}} & \sin \phi_n &= \frac{-q}{(p^2 + q^2)^{1/2}}\end{aligned}$$

Figure 7 is an isometric plot of the area, and figure 8 is an image of the area generated by translating altitude into brightness. The image is accompanied by a histogram of altitudes present in the DEM. The solid histogram represents targets that are sunlit, while the shaded one represents targets that are shadowed. This presentation form is used throughout the paper: image on the left, histogram of image values on the right with sun and shadow distinguished. The solid histogram sits on top of the shaded one; that is, the top of the solid histogram is the sum of sunlit and shadowed values for that altitude.

One multispectral image consisting of four spectral bands from Landsat 1 was obtained for the given area. The image, number 1078-09555, was acquired about 9:55 a.m. GMT on October 9, 1972. (Table 1 lists relevant orbital and sensor data for Landsat 1.) For the experiments described below, only MSS band 4 was used. During the overflight, the sun was at an elevation of 34.2° with an azimuth of 154.8° , corresponding to an incident solar direction (θ_0, ϕ_0) given by $\cos \theta_0 = \cos(90^{\circ} - 34.2^{\circ}) = 0.562$, $\phi_0 = 295.2^{\circ}$ counterclockwise from the

global x -axis (geographic east). The Landsat image was registered with the digital elevation model [20], and radiometric corrections were applied to eliminate striping [33]. Figure 9 shows the actual MSS band 4 as used in the experiments. Cast shadow information for the given sun position was generated by the application of a hidden surface display algorithm [40]. The resulting shadow masks, one for cast shadows and one for self shadows, are shown in figure 10. Figure 11 is a synthetic image of the area. The image is how the surface would appear at the time of the overflight if the surface were a perfect Lambertian reflector of unit albedo and there were no intervening atmosphere [19].

3.2. Difficulties with Parameter Fitting

It is tempting to adopt a parameter-fitting technique based on minimizing some error function, but such a method is fundamentally flawed. One could assume an approximate albedo map for a given surface, based perhaps on the values obtained by assuming no atmosphere. The albedo at each target (x_t, y_t) could be estimated from the recorded satellite radiances $L(x_t, y_t)$:

$$\rho(x_t, y_t) = \frac{\pi L(x_t, y_t)}{E_0 R(\theta_n, \phi_n)}$$

where (θ_n, ϕ_n) gives the target's orientation. This initial albedo description could be used, for example, in least-squares minimization to determine the model parameters. The relevant error is $\xi = \sum(L_m - L)^2$, where L_m is the model radiance and the sum is over every element in the image (alternatively, every target in the scene). The model radiance L_m is a function of the six unspecified parameters and the set of target albedos provided by the initial albedo estimates. The error ξ is locally minimized when $\partial\xi/\partial X = 0$ for each of the six parameters X . A solution to the resulting system of six equations yields trial values for the parameters, which are then used to generate another albedo image, and the minimization process is repeated.

There are two objections to this scheme, one computational, the other fundamental. The system of six equations to solve are very nonlinear, and terms are coupled due to the multiplicative transmission factors. No general solution has been found, although gradient descent methods can be applied [41]. An approximate solution can be obtained by linearizing the imaging equation: expand the exponentials in their power series form and ignore terms beyond the linear. The error ξ is then a quadratic, and reliable techniques are available for its solution. But even this approach is limited.

The essential problem is that no new information is introduced into the process beyond specifying the initial set of albedo values. For any albedo map, the parameter values delivered by minimizing the error ξ are precisely those that best match the given map. There is no reason to expect iteration to produce an albedo image that is any better than the first one. Before the kind of parameter fitting described here can be applied, assuming that it will work at all, additional independent information must be available.

3.3. Information Sources External to the Image

3.3.1. Optical Depth

If no other data is available, a good starting model of optical depth is provided by the U.S. Standard Atmosphere. As mentioned previously, the USSA was devised to facilitate research in atmospheric optics. It tabulates particle number density and size, air pressure, and temperature at a range of altitudes for the earth [34,35]. From these tabulations, the optical depth can be computed for any altitude. In the amended version, a set of five regional standard atmospheres was established: subarctic summer, subarctic winter, midlatitude summer, midlatitude winter, and tropical [42]. Figure 12 shows the variation in optical depth with altitude for the two principal attenuating components, molecules and aerosols (ozone absorption is neglected here), and for their sum. The data is for a wavelength of 550 nm, corresponding to the center of Landsat MSS band 4 [34].

An optical depth model consisting of a single exponential component rather than the sum of two is more convenient theoretically, and makes little difference computationally. An optical depth like the USSA that is the sum of two exponentially-varying components requires four independent parameters. The resulting transmission is a product of two factors: $T = e^{-\tau_A - \tau_R} = T_A T_R$. The single-component model requires only two parameters, and transmission becomes a single factor: $T = e^{-\tau}$. The optical depth model used in the present investigation was such an approximation to the sum of Rayleigh (molecular) and aerosol components from the USSA. Figure 13 shows exponential forms fitted to the tabulated data for the two components separately and for their sum. The parameters of the exponential curves are:

$$\begin{array}{lll} \text{Rayleigh:} & \tau_{0R} = 0.09917 & H_R = 8232 \text{ m} \\ \text{Aerosol:} & \tau_{0A} = 0.19 & H_A = 1211 \text{ m} \\ \text{Sum:} & \tau_0 = 0.2619 & H = 2529 \text{ m} \end{array}$$

Both the tabulated USSA and exponential forms, implemented by table look-up, were used in generating albedo maps. There were no detectable differences in the resulting pairs of albedo images.

3.3.2. Path Radiance and Sky Irradiance

There are no standard models for sky irradiance or path radiance. However, a number of theoretical and experimental studies have accumulated data for both. The Turner-Spencer and Otterman computational models have already been mentioned. Data from these and the compilation of Coulson, Dave, and Sekera [43] are presented in table 2 (path radiance) and table 3 (sky irradiance). All three studies assumed a horizontally homogeneous atmosphere bounded by a horizontal Lambertian surface of albedo ρ . The values in tables 2 and 3 are for the wavelength interval 500-600 nm, corresponding to Landsat MSS channel 4. The extraterrestrial solar irradiance in this band is assumed to be 17.7 mW cm^{-2} [45], and the solar zenith angle θ_0 is such that $\cos \theta_0 = 0.6$.

Experimental measurements for extraterrestrial solar irradiance, atmospheric transmission, optical depth (inferred from the measured transmission), sky irradiance, path radiance, and related quantities are variously shown in table 4. Values are given for the spectral intervals corresponding to all four Landsat MSS channels.

The first part of the table gives the extraterrestrial solar irradiance from three sources. E_0 is the irradiance falling on a surface of unit area oriented toward the sun (its surface normal points at the sun), measured outside the terrestrial atmosphere. The data in the first line is from Chapter 16 of Valley's book [34], converted into mW cm^{-2} . It is simply the reported solar irradiance values for each wavelength interval summed over the appropriate Landsat band limits. The second line is from Thekaekara's [45] tabulation, which is a commonly used source of solar irradiance data. This data was averaged by integrating the solar spectrum irradiance at each tabulated wavelength, weighted by the nominal Landsat spectral response curves. The data from Rogers [46] in the third line is from RPMI (Radiant Power Measuring Instrument) ground measurements, corrected for transmission.

The second part of the table lists the nominal sea-level optical depth for the U.S. Standard Atmosphere [34], molecular, aerosol, and ozone components, as well as reported values from Rogers [46] and Ahern, Teillet, and Goodenough [47]. The transmissions for the U.S. Standard Atmosphere were computed from the Valley optical depths, $T_u = e^{-\tau}$. The transmissions for the Rogers and Ahern data are the ratios of the measured solar irradiance to E_0 , corrected for slant path; the given optical depths were inferred from these transmissions.

Rogers and his colleagues made simultaneous satellite, aircraft, and ground readings over a fairly flat region of Michigan, elevation about 290 meters. The solar zenith angle was $\theta_0 \approx 48.0^\circ$. All measurements were reported to be on clear days.

The values taken from Ahern *et al.* [48] are for what he and his colleagues termed "standard conditions." The data is from a collection of observations made May through September 1976 over a portion of the Canadian Shield north of Ottawa. The area was fairly flat and characterized by abundant clear lakes. The altitude of the places where ground measurements were made was not reported. The solar zenith angle in the standard conditions was $\theta_0 = 40.0^\circ$, and all measurements were reportedly made on clear days. The final entry in the table gives the average background albedo for each Landsat band, as formulated in the standard conditions.

3.4. Information Sources Within the Image

The theoretical and experimental data described above provide a starting point for the determination of model parameter values that yield the best albedo maps. They also serve as a useful check on the values subsequently determined. But they do not reflect the character of a particular scene under consideration. It is generally desirable to use as much information from the image as possible.

3.4.1. Use of Calibration Targets

The presence of targets of known albedo in the scene is very useful. Such calibration targets have been investigated as aids to determining path radiance. Ahern *et al.* [48] used clear lakes of low albedo as black reflectors, and equated the measured sensor radiance over such targets with the path radiance. Provided clear lakes appear over a wide range of altitudes, this technique could be applied profitably in mountainous terrain. Regrettably, the Dent de Morcles region in Switzerland used in the present study did not satisfy this requirement: there were few lakes of sufficient clarity and they were not distributed throughout the scene's elevation range. No other targets of known albedo (for example, large areas of blacktop or dark tilled soil) were present.

3.4.2. Using Shadows to Calibrate the Image

Shadows provide another kind of calibration target. Piech and Schott [49] used shadows advantageously in densitometric studies of specular and diffuse reflection from lake surfaces. A linear relationship exists between the scene radiance from sunlit areas and that from areas in cast shadow. By computing the relationship's slope and intercept values, they were able to recover path radiance over the lakes as well as sky irradiance. There was no attempt to compare lake surfaces at different altitudes or non-horizontal surfaces.

In more recent work, Woodham [21] has examined the differences between sunlit and shadowed targets in Landsat images of a lake and a flat area of coniferous forest in British Columbia. He specifically points out the variation of path radiance with elevation as can be seen by altitude profiles of the sensor radiance.

Shadows are especially attractive in that they exist at nearly every altitude in mountainous terrain and can provide elevation-dependent information. They are especially prevalent in Landsat images due to the early morning overflight and consequent low sun elevation. Although it is possible under certain conditions to determine target albedo using shadows, they are more useful in finding path radiance.

In certain circumstances, it is possible to estimate the albedo of the surface where there are nearby sunlit and shadowed targets. Consider two neighboring targets separated by a cast shadow boundary. Let target 1 lie in the sun, target 2 in shadow, and make the following assumptions:

1. both targets are at the same altitude, z ;
2. they have similar surface orientations, $(\theta_{n1}, \phi_{n1}) \approx (\theta_{n2}, \phi_{n2})$;
3. they share a common albedo, ρ ;
4. the optical depth of the targets is known.

Then the difference between the measured radiance from the two targets is due to the reflected solar irradiance from the sunlit element:

$$\begin{aligned}
L_{m1} - L_{m2} &= [L_{t1}T_u + L_p] - [L_{t2}T_u + L_p] \\
&= \frac{\rho}{\pi} [E_0 R(\theta_{n1}, \phi_{n1}) T_d(z) + E_s(z) \frac{1}{2} (\cos \theta_{n1} - \cos \theta_{n2})] T_u(z) \\
&\approx \frac{\rho}{\pi} E_0 R(\theta_{n1}, \phi_{n1}) T_u(z) T_d(z)
\end{aligned}$$

(The function arguments have been omitted in the first line.) The differential sky irradiance is small since $\cos \theta_{n1} \approx \cos \theta_{n2}$. E_0 and $R(\theta_{n1}, \phi_{n1})$ are known and $T_u(z)T_d(z)$ is computed from optical depth. Inverting this expression and using measured sensor values L_1 and L_2 gives the albedo estimate:

$$\rho \approx \frac{\pi(L_1 - L_2)}{E_0 R(\theta_{n1}, \phi_{n1}) T_u(z) T_d(z)}$$

A representative albedo for a small area can be obtained by averaging over sunlit/shadowed target pairs in the area. The Dent de Morcles region was subjected to the analysis suggested here, but with limited success. As discussed below, accumulated errors in the resampled image and inaccuracies in the digital elevation and slope models lead to widely-varying and unreliable albedo values.

Shadows are especially useful in obtaining information about path radiance. Figure 14 is an altitude profile of minimum sensor radiance over the test region. These minima occur almost entirely in shadowed targets. If one assumes that the minimum radiances are from shadowed targets with very small albedo, then the profile of figure 14 approximates the path radiance function $L_p(z)$. By fitting an exponential curve to the profile, one determines possible values of the parameters L_{p0} and H_p . Two similar exponential curves are superimposed on the minimum sensor radiance profile in figure 15.

One must be careful when fitting model path radiance curves to the minimum sensor data. The model function is exponential, decreasing monotonically with altitude. Although the points in figure 14 clearly drop off with elevation in the early part of the graph, the trend reverses at higher z . This increase is expected since there is a definite increase of average albedo with altitude as computed by examining sunlit targets due to the presence of snow (figure 16). Even in shadow, the minimum radiance is substantial. The high albedo of snow means that reflected skylight and the effects of mutual illumination cannot be neglected. When fitting the model curve, it is necessary to use sensor radiances from targets only up to some arbitrary maximum altitude and ignore those beyond.

Fitting path radiance to minimum sensor data requires satisfying physical constraints as well as choosing the data carefully. The exponential curves must lie entirely below the sensor radiance values, since path radiance cannot be negative. One cannot therefore try to fit an exponential through the data by least-squares. The two curves of figure 15 were both fitted by hand.

The form of figure 14 does not itself suggest an exponential form of path radiance any more or less than it does a linear form. Figure 17 compares one linear model with the exponential. For low values of z , they agree reasonably well. The particular linear model shown, $L_p(z) = A(1 - z/B)$, was obtained by linearly approximating the exponential:

$$A(1 - z/B) \approx L_{p0}(1 - z/H_p)$$

$$A = L_{p0}, \quad B = H_p$$

However, the exponential model is more faithful to the true character of path radiance and is not substantially more difficult to compute. It is defined for all altitudes z , unlike the linear form which must be set to zero when $z > B$.

Sky irradiance estimates, particularly the variation with altitude, are very hard to make. The presence of snow-covered targets in shadow suggests a possibility. If suitable optical depth and path radiance models are assumed, and snow albedo is estimated at perhaps 0.90, then a very coarse value for E_s can be obtained for a target at altitude z with sensor radiance L :

$$E_s(z) \approx \frac{\pi(L - L_p(z))}{\rho T_u(z) h(\theta_n, \phi_n)}$$

where $h(\theta_n, \phi_n) = \frac{1}{2}(1 + \cos \theta_n)$, the geometric factor for a hemispherical sky, $\rho = 0.90$, and $T_u(z)$ and $L_p(z)$ are presumed known. If several such values are obtained over a range of altitudes, then E_{s0} and H_s can be estimated.

However, the estimates are not reliable. They depend on accurate models of optical depth and path radiance. They are particularly sensitive to variations in $L_p(z)$, since the term $(L - L_p(z))$ is usually small. They also depend on knowing $h(\theta_n, \phi_n)$ accurately, and as already mentioned, the digital slope model for the test region had large errors. As a result, this method of estimating sky irradiance was not especially useful. An alternative procedure based on trial-and-error was adopted.

4. Generation of Albedo Images

The success of the methods explored above rely heavily on the quality of the data used. It is possible to obtain reliable estimates of path radiance from the altitude profile of minimum sensor radiance values. The exponential curve fit depends only on the satellite image data and is relatively tolerant of noise, although one must be careful to use only values for altitudes below a certain maximum. On the other hand, computing albedo using the difference in sensor radiance between targets straddling cast shadow boundaries does not yield reliable values. These estimates are very sensitive to inaccuracies in the topographic models—the elevation data originally supplied and the slope and shadow models generated therefrom—as well as errors in the path radiance model. Because the satellite image had been resampled during rectification, the sensor values for nearby sunlit and shadowed targets were smeared together. Similarly, an estimate of sky irradiance for shadowed snow-covered targets depends strongly on the accuracy of the slope of the surface, as well as the accuracy of the path radiance model and the assumption of the hemispherical nature of the sky. Since noisy conditions are the rule rather than the exception in remote sensing, a better method was sought to determine the parameters of optical depth and sky irradiance.

The method discussed presently is based on trial and error. One makes an educated guess for the atmospheric model parameter values and generates an albedo image using these values. By applying a set of subjective criteria, the acceptability of the image as an albedo map is determined. One can then refine the model parameter values, generate another image, and reapply the criteria. This process, while admittedly a bit of an art, has been found to produce an acceptable albedo map.

4.1. Criteria for a Good Albedo Image

An albedo image ideally represents the spatial variation of surface albedo over the scene. With this in mind, three subjective criteria were established in order to judge the quality of albedo maps generated as described above. The qualities examined include (1) the presence of shading artifacts due to shape, (2) the match in albedo between sunlit and shadowed regions, and (3) the dynamic range of computed albedo.

There should be no visible evidence of surface shape (topography) that results from the imaging process. One expects the ground cover to change with elevation as the nature of the surface material changes. On occasion, it may even change with surface aspect (azimuth of the surface normal); for example, vineyards tend to be planted on south-facing slopes more than north-facing. But there should be no shading difference between targets of like albedo and different orientations.

The computed albedo between sunlit and adjacent shadowed targets should be comparable, with no evidence of shadows. This is especially true if the shadow is cast by some nearby topographic feature. The boundary of such a shadow arbitrarily cuts across a region that is probably more or less homogeneous, that is,

of similar elevation, surface slope, and ground cover on both sides of the boundary. Any substantial deviation in albedo is probably due to an inaccurate atmospheric model, although bad image and topographic data also contribute.

Finally, the dynamic range of the computed albedo set ought to be reasonable. If the imaging equation and the model underlying it were exact, and the data were precise and error-free, then every albedo calculated would lie between 0.0 and 1.0. Unfortunately, such ideal conditions are rarely realized in practice. A certain percentage of targets will have apparent albedo outside the physically possible range. The remainder should be distributed mostly within the range expected for natural surfaces of the kind being observed: a few percent for clear lakes and dark fields or dense forest, and perhaps 90-95% for snow-covered slopes.

These criteria were used to judge synthetic albedo images generated from a number of parameter sets. Three such images are presented below to illustrate the process.

4.2. Model A

For comparison, the first model presented is based on the Turner-Spencer calculations of path radiance and sky irradiance. Normally, measured visibility is used to obtain aerosol optical depth. From this and the standard value for molecular optical depth, a forward-scattering parameter η is computed. Since no visibility measurements were available for the Dent de Morcles test area, the U.S. Standard Atmosphere aerosol as well as molecular optical depths were used [30]:

$$\eta = \frac{0.5\tau_R + 0.95\tau_A}{\tau_R + \tau_A} = 0.796 \quad (14)$$

Here, $\tau_R = 0.09917$ and $\tau_A = 0.19$ are taken from the exponential forms fitted to the USSA values. Using the USSA sea-level numbers themselves results in $\eta = 0.792$, a difference of only a half percent. Scattering was presumed to be dominated by the molecular component and a Rayleigh single-scattering phase function was used. An average background albedo of $\bar{p} = 0.15$ and an extraterrestrial solar irradiance of $E_0 = 17.7 \text{ mW cm}^{-2}$ were assumed. Transmission was computed using the exponential optical depth fitted to combined Rayleigh and aerosol USSA values. The resulting path radiance and sky irradiance on a horizontal surface are exhibited in figure 5 and figure 6 respectively.

There are several noteworthy features of the albedo image made using this model (figure 18). Certain areas that appear quite bright in the original Landsat MSS band 4 image are muted in the albedo image. This is particularly so of the snow-covered mountains in the northeast (upper left) corner and of the clouds in the northwest corner. It is well-known that the MSS sensors aboard the Landsat satellites unfortunately saturate on snow, clouds, and other highly reflective surfaces in sunlight. Consequently, the recorded radiances are less than they should be, and the computed albedo is too low.

A second fact is that it is quite easy to distinguish shadowed from sunlit areas. The shadowed areas are brighter, that is, have a higher albedo than neighboring

regions in sun. This is emphasized in the histogram to the right of the image: the peak for shadowed targets lies to the right of the peak for sunlit targets, although not as pronounced. This difference is clear in the enclosed valley in the left center of the image. The east shadow boundary running through the middle separates sun on the left from shadow on the right. This distinction between shadows and sunlit areas violates the second of the criteria set forth above for an acceptable albedo map. It is possible to improve the image by adjusting the six model parameters appropriately.

Figure 18 is a test image of interest, and one that suggests how to modify the model parameters to account for the apparent increase with elevation of albedo in shadows. The albedo values for slopes of the southeast ridge bounding the central valley lie in the range 0.20-0.30. At the valley center, the computed albedo is about 0.25-0.30. It increases with elevation and with slope to 0.80-0.90 just below the ridge crest. This contrasts with the slopes to sun of the valley, where the sunlit southeast-facing slopes show albedo values of 0.20-0.30. The albedo has a more or less uniform value of 0.20-0.30. A small precipitation can be seen in the vicinity of the summit of Dent de Morcles and other places in the image.

The behavior of the computed albedo in shadow suggests that the elevation dependence of the path radiance or sky irradiance components, or both, may be wrong. The generally larger shadow albedo indicates that perhaps too little path radiance is being removed. A larger value would reduce shadow albedos while affecting sunlit target albedo less (the relative contribution to sensor radiance of reflected sunlight is about twice that of path radiance for a horizontal surface under the conditions assumed here). By increasing the scale height H_p , the path radiance is made larger at higher elevations.

A similar argument applies to sky irradiance. By increasing the scale height H_s , the irradiance from skylight is larger with altitude and results in smaller computed albedo. The relative contributions of reflected skylight to path radiance to reflected sunlight for the conditions assumed here is about 2:5:9 respectively. Thus increasing sky irradiance makes only a small difference in most computed sunlit albedo values, while substantially decreasing those for shadowed targets.

4.3. Model B

The second albedo image presented incorporates the modifications mentioned above and is an improvement (figure 19). The set of model parameters included the same optical depth as used in model A, but different path radiance and sky irradiance parameters. Both the sea-level value L_{p0} and scale height H_p for path radiance were taken from the exponential model fitted to minimum scene radiances as discussed above. L_{p0} was actually reduced by 16%, but H_p was increased by 72% over its value in model A. Sea-level sky irradiance was rounded down very slightly, and the scale height was taken to be the same as for path radiance. Lacking other data, this was a reasonable assumption.

The parameters of optical depth were not changed in this model. Experiment showed that for the low optical depth values required for the test region, the

albedo image was relatively insensitive to moderate changes in the sea-level value or scale height. Optical depth is also more reliably determined from transmission measurements, so there is reason to place more faith in the optical depth values than in path radiance or sky irradiance.

The criteria for a satisfactory albedo image are better met by this model than the previous one. The appearance of shadowed areas in the image more closely matches that of adjacent sunlit areas, although there is still some disparity. The histogram of shadow albedo more closely parallels that of sunlit albedo, and there are fewer overflow values (rightmost histogram bin). It is noteworthy that the albedo range in this second model is somewhat less than that of the first, especially for shadowed targets. Also, while the average albedo for sunlit targets has diminished by only 6%, that for shadowed targets has been reduced by 28%.

There is some evidence that the albedo gradient observed on shadowed northeast-facing slopes may actually be a property of the scene. The gradient in figure 20 appears to have been reduced from that in figure 19, but it is still present. The division between the brighter, higher area and the darker valley floor is fairly distinct, and each area appears roughly homogeneous. The larger albedo may indicate the presence of moderately reflective surface material such as unvegetated rock, perhaps interspersed with snow. The south-facing slope is exposed to more sun and may support more vegetation and less snow. This is one example of an aspect-dependent effect that should be preserved in the albedo image, since it is a true property of the surface.

4.4. Model C

The third and final albedo image presented improves somewhat on the previous two. Path radiance scale height and both sky irradiance parameters were maintained from model B. Sea-level path radiance was increased to a value intermediate to that of either previous models in an effort to decrease shadow albedo over that computed in model B. To partially compensate for reducing the sunlit albedo, the optical depth parameters were also changed: sea-level optical depth was decreased 12%, while scale-height was increased 58%. The change in optical depth in effect simulated a clearer atmosphere (less aerosol) than the USSA.

As a result of these modifications, the albedo image (figure 20) shows marginally better agreement between sunlit and shadowed target albedos, although it may be difficult to see through the photographic reproduction process. In particular, the albedo histograms for the two are similar.

In terms of the criteria established for judging albedo images, model C performs well, although further tuning the parameters could probably improve it. If one compares the albedo image in figure 20 with the synthetic image in figure 11, it is apparent that virtually all shading due to varying topography has been obliterated. The match between sunlit and shadowed target albedo is very good. One notes that the boundaries between sun and shadow are evident as strings of dark targets. These are the result of noise in the digital elevation model and the calculation of the location of cast shadows. Finally, the range of computed albedo fits will

within the physically required range, for sunlit and shadowed targets individually and together, and their respective histograms agree well.

4.5. Qualitative Effects of Changing Model Parameters

A series of experiments was performed on the individual effects of extreme parameter values on the generated albedo images. The parameters from model B were taken as the basis for synthesizing six new pair of albedo maps, each pair representing one of the six model parameters. One of each pair of images was made with a high value for the corresponding parameter, and the other was made with a low value. Table 5 displays the parameters used for each of albedo images D1 through D12, which are shown in figure 21.

The albedo of the target at (x_t, y_t) that has a recorded sensor radiance $L(x_t, y_t)$ is obtained from eq. (13) by substituting in the model functions for transmission, path radiance, and sky irradiance:

$$\rho(x_t, y_t) = \frac{\pi[I(x_t, y_t) - L_{p0}e^{-z/H_p}]}{E_0 R(\theta_n, \phi_n)e^{-\tau(z)/(1+1/\cos\theta_0)} + E_{s0}e^{-z/H_s}h(\theta_n, \phi_n)e^{-\tau(z)}} \quad (15)$$

By inspecting the signs of the partial derivatives of ρ with respect to the six parameters τ_0 , H , L_{p0} , H_p , E_{s0} , and H_s , one finds that the sensor radiance increases with increasing τ_0 and H , and decreases with increasing L_{p0} , H_p , E_{s0} , and H_s . The series of experiments confirms this qualitative analysis. Increasing the optical depth scale height has a more pronounced effect on the dynamic range of the computed albedo than increasing the sea-level optical depth. There is no discernible effect on discriminating shadowed and sunlit targets.

Changing the sky irradiance parameters has a marked effect on the albedo computed for the shadows, of course, while hardly affecting that for sunlit targets. Decreasing the sea-level sky irradiance raises the computed albedo in shadows significantly. The effect of a decrease in the scale height is most noticeable on the shadowed slope of a steep ridge, as pointed out earlier. The top of the ridge appears highlighted, and the albedo decreases rapidly with decreasing elevation. Such a rapid decrease is probably not a property of the surface cover and indicates that the scale height may be too low. However, for the particular scene examined here, there appears to be a genuine change in surface albedo.

The most important effect on the image in both sunlit and shadowed targets is the path radiance. Increasing L_{p0} simply shifts the dynamic range of albedo by an amount that varies with elevation, the shift less at high altitude. The effect on shadows is greater than the sunlit areas. One must monitor the number of values that underflow (computed $\rho < 0$), and adjust the path radiance downward if there are too many because too much path radiance was subtracted. Reducing the scale height makes the shadow albedo much larger, especially at higher elevations, because the path radiance more closely approximates a constant instead of dropping off with altitude.

5. Summary

Intrinsic properties of the earth's surface can be reliably recovered from remotely-sensed images, but only if the imaging process is suitably understood. In optical sensing of mountainous terrain, a model of the imaging process must include the effects of surface topography and, at least in the shorter wavelengths, the effects of the atmosphere. Surface reflectance can be written as a function of sensor radiance, target irradiance, and path radiance by inverting the image-forming equation that represents the imaging model. This is in general very difficult to do. By adopting some reasonable restrictions, a simple but adequate equation describing the radiance reaching the satellite sensor can be developed and inverted to obtain target albedo. The parameters of the model can be obtained partly from image data and partly by educated guessing and trial and error. The model can then be applied to the satellite data to obtain useful representations of surface cover in the form of an albedo map.

Applications in the visible spectrum of remote sensing from high-altitude craft must reckon with the atmosphere to obtain reliable information about the surface. The effects become complex in mountainous terrain for two reasons. First, the quantity of air interposed between the sun and target and again between the target and sensor varies significantly across the image as the surface elevation changes. This affects the amount of incident sunlight and skylight reaching the surface, the transmission of reflected target light that reaches the satellite, and the amount of spurious light scattered into the sensor. Second, the surface is characterized by a wide range of slopes which affects the amount of target irradiance from sun and sky. To correctly recover the target albedo, an adequate model of the sensor radiance, expressed as the satellite image-forming equation, and its dependence on the atmosphere is essential.

An accurate analysis requires extensive mathematical treatment, which so far has been accomplished only numerically and for a small number of special cases. By making certain assumptions, a simple image-forming equation was developed and inverted to obtain surface reflectance (represented by albedo) as a function of six model parameters. The atmosphere is assumed to be semi-infinite, plane-parallel, and horizontally homogeneous. The surface is assumed to be a Lambertian reflector, where the albedo may vary point to point. The sun is a point source at infinity, and the satellite is a point observer at infinity directly over the imaged area. It is also assumed that the sun and sky are the only target illuminants, and that the sky can be modeled as a uniform hemispherical source. Under these assumptions, the image-forming equation is considerably simplified to the form shown in eq. (11).

The simplified image-forming equation involves four atmospheric quantities, all depending on altitude:

- $T_d(z)$, the transmission of the solar beam to the surface at elevation z ;
- $T_u(z)$, the transmission of the target radiance to the satellite;
- $E_s(z)$, the irradiance of a horizontal target at z by the sky;

$L_p(z)$, the path radiance.

Transmission is the easiest component to handle once optical depth has been introduced: $T_u(z) = e^{-\tau(z)}$ and $T_d(z) = e^{-\tau(z)/\cos\theta_0} = [T_u(z)]^{1/\cos\theta_0}$. The sky irradiance and path radiance may be arbitrarily complex, depending on the accuracy required of the model. For the present study, exponential forms were assumed since this form matches that of more carefully computed theoretical models:

$$\begin{aligned}\tau(z) &= \tau_0 e^{-z/H} \\ L_p(z) &= L_{p0} e^{-z/H_p} \\ E_s(z) &= E_{s0} e^{-z/H_s}\end{aligned}$$

Under all these assumptions, target albedo is easily obtained (eq. (15), repeated here):

$$\rho(x_t, y_t) = \frac{\pi[L(x_t, y_t) - L_{p0}e^{-z/H_p}]}{E_0 R(\theta_n, \phi_n) e^{-\tau(z)/(1+1/\cos\theta_n)} + E_{s0} e^{-z/H_s} h(\theta_n, \phi_n) e^{-\tau(z)}}$$

$R(\theta_n, \phi_n)$ accounts for shadowing and for the foreshortening of the surface with respect to solar incidence, and $h(\theta_n, \phi_n) = \frac{1}{2}(1 + \cos\theta_n)$ accounts for the uniform hemispherical sky. Once the six atmospheric parameters have been determined, target albedo can be computed and represented by an albedo map.

Some methods for determining certain of the model parameters were explored. Published theoretical and experimental values provide a starting point, but do not relate to a particular image. If targets of known albedo at a range of altitudes are present in the scene, then it is possible to determine values for the atmospheric parameters. Such calibration targets were not available for the Dent de Morcles region, but shadowed targets could also serve. It is possible to obtain reliable estimates of path radiance from the altitude profile of minimum sensor radiance values, assuming only that the targets with minimum radiance correspond to shadowed areas of low albedo. On the other hand, an attempt at finding albedo using the difference in sensor radiance between targets straddling cast shadow boundaries was unsuccessful. An attempt at computing sky irradiance based on radiance from shadowed snow-covered targets also failed. The latter two methods are quite sensitive to noise in both the satellite image and the digital terrain models used to represent surface topography.

In view of the noisy conditions normally present in current satellite imaging and the small dynamic range of discrete sensor signal values, an alternative means of determining the model parameters was presented and shown to work acceptably. For a given set of model parameters, an albedo image may be examined directly and evaluated according to subjective criteria of acceptance. The primary requirement of a satisfactory albedo image is that it is invariant with respect to the imaging situation and the surface topography. There should be no effects of elevation except those inherent in the properties of the surface cover, no shading of hillslopes, and no shadows (cast or self). Targets on either side of the border between sunlit and shadowed targets probably have similar albedo and should appear the same. A histogram of the albedo image should be contained entirely within the range of 0.0

to 1.0, and its shape and mean albedo value should be consistent with whatever is known about the type of area imaged. Although these criteria are not often met in practice, useful results can still be obtained.

A number of synthetic albedo images were generated and evaluated as to their acceptability. Three of these were presented to illustrate the application of the subjective criteria. In addition, a separate set of twelve albedo images was synthesized to systematically investigate dependence on the atmospheric parameters. Of the three illustrated here, model C seems to be the best. It may be difficult to distinguish albedo image C and albedo image B after the reproduction process. Even though their histograms are quite similar, there is sufficient disparity to favor the model C. There is a better match in model C between the distributions of shadow albedos and sunlit albedos than in model B. It remains to be seen how the use of albedo images as input to classification systems affects the subsequent analysis of surface cover in mountainous terrain.

6. Conclusions

Several facts emerge from the experiments performed in the course of the research. First, it is clear that the atmospheric radiometric quantities vary with elevation, especially path radiance, so that altitude dependence must be included in any reasonable model.

Second, a simple imaging model can approximate atmospheric effects sufficiently well to generate reasonable albedo maps for mountainous terrain. Values of the model parameters can be obtained by trial generation of albedo images and subsequent subjective evaluation.

Third, although the presence of specific calibration targets in the scene would simplify the determination of parameter values, shadows may be used almost as effectively. Path radiance as a function of altitude can be successively computed this way. But subjective evaluation is still necessary to assist in finding suitable values for the other components.

Fourth, in the process of improving model parameters, the albedo image shows itself to be a useful tool. The albedo image presents one aspect of an intrinsic surface property in a form immediately comprehensible for humans. It is an effective aid in determining how the model parameters should be set to obtain an acceptable final representation.

Fifth, the albedo images appear to be more sensitive to the path radiance parameters than to those of either optical depth or sky irradiance. The radiance of shadowed targets and sunlit targets near grazing solar incidence is quite sensitive to changes in the sky irradiance, since the radiance from the shadows is small to begin with. Yet changes in the path radiance parameters strongly affect every computed target albedo in the scene.

Sixth, the optical depth parameters τ_0 and H appear to control the dynamic range of the albedo image. One notices a substantial widening of the histogram when either parameter is increased.

Seventh, the presence of an atmosphere actually increases the information available in the satellite image. Without the distributed sky irradiance, one could not compute the albedo of targets in shadow. Indeed, an examination of images from Landsat bands 6 and 7 (near infrared) shows black shadows, with radiance essentially zero. On the other hand, there is no path radiance to mask the reflected target radiance. Designers of future earth sensing satellites must carefully consider these two competing issues when deciding the spectral bands to use, especially if the satellites are expected to perform well in mountainous areas where shadows abound.

To obtain accurate information about the surface from remotely sensed images, a good model of atmospheric and topographic effects is essential. A digital terrain model can provide elevation and slope information, but atmospheric effects are more difficult to ascertain. This paper describes one way to obtain a simple model based on only six parameters. The methods for determining the parameters are

approximate, and the values obtained need to be tuned by subjective evaluation of albedo images. It seems imperative that if future earth resources satellites are to achieve their full potential, they must provide some assistance in determining the model parameters by making whatever measurements are necessary and possible.

The simple model presented in this paper appears adequate to correct images of rapidly varying terrain for atmospheric influences. It is difficult to objectively evaluate the images presented here due to the lack of ground truth. The rectified and destriped satellite image and the digital terrain model contain a good deal of noisy or corrupted data. However, the model as used here is not particularly sensitive to the kind of errors present in the data. The effects of some of the errors undoubtedly have been averaged away within the coarse nature of the model. In return for this tolerance, detailed information about surface reflectance and atmospheric properties has been discarded. As the input data becomes more accurate, the model must keep pace. One must be prepared to relax the assumption that the sky is a uniform hemisphere and take into account its true radiance distribution. Provision must be made for identifying bad data, for example, ignoring the targets lying beneath clouds. More accurate models require more information, including perhaps detailed measurements of atmospheric composition. It may be possible, however, to avoid such tedium by the judicious use of calibration targets in the scene itself. The presence of targets of known albedo makes an optimization procedure feasible and attractive. In any case, the removal of atmospheric and topographic effects from data is essential before more advanced scene interpretation methods, such as the context-guided region merging introduced by Starr and Mackworth [50], can be applied.

7. References

1. J. N. Howard and J. S. Garing, Atmospheric optics and radiative transfer, *Trans. Am. Geophys. Union*, **52**, 371-389 (1971).
2. E. J. McCartney, *Optics of the Atmosphere: Scattering by Molecules and Particles*, (John Wiley & Sons, New York, 1976).
3. G. V. Rozenberg, Light scattering in the earth's atmosphere, *Soviet Phys. Usp.*, **3**, 346-371 (1960).
4. A. J. LaRocca and R. E. Turner, *Atmospheric Transmittance and Radiance: Methods of Calculation*, IRIA State-of-the-Art Report, ERIM 107600-10-T (Environmental Research Institute of Michigan, Ann Arbor, MI, 1975).
5. J. B. Pollack, Rayleigh scattering in an optically thin atmosphere and its application to Martian topography, *Icarus*, **7**, 42-46 (1967).
6. A. T. Young, High-resolution photometry of a thin planetary atmosphere, *Icarus*, **11**, 1-23 (1969).
7. R. M. Hoffer and staff, *Natural Resource Mapping in Mountainous Terrain by Computer Analysis of ERTS-1 Satellite Data*, LAIRS InfoNote 061575, (Laboratory for Applications of Remote Sensing, Purdue University, W. Lafayette, IN, 1975).
8. S. I. Solomon, J. Cameron, J. Chadwick, and A. S. Aggarwal, Use of topographic data on land-use land-cover delineation by ERTS imagery, in *Proc. 2nd Symp. Machine Processing of Remotely Sensed Data*, (Laboratory for Applications of Remote Sensing, Purdue University, West Lafayette, IN, 3-5 June, 1975), p. 4B-1.
9. M. D. Fleming, J. S. Berkebile, and R. M. Hoffer, Computer-aided analysis of Landsat-1 MSS data: a comparison of three approaches, including a "modified" clustering approach, in *Proc. 2nd Symp. Machine Processing of Remotely Sensed Data* (Laboratory for Applications of Remote Sensing, Purdue University, West Lafayette, IN, 3-5 June, 1975), p. 1B-54.
10. F. G. Sadowsky and W. A. Malila, *Investigation of Techniques for Inventorying Forested Regions. Vol. 1: Reflectance Modeling and Empirical Multispectral Analysis of Forest Canopy Components*, Final Report, NASA-CR-151561 (1977).
11. B. N. Holben and C. O. Justice, The topographic effect on spectral response from nadir-pointing sensors, *Photo. Eng. Rem. Sens.*, **46**, 1191-1200 (1980).
12. B. K. P. Horn, chapter 4 in *The Psychology of Computer Vision*, P. H. Winston, ed., (McGraw-Hill, New York, 1975).
13. R. J. Woodham, Reflectance Map Techniques for Analyzing Surface Defects in Metal Castings. Technical Report TR-457 (Artificial Intelligence Laboratory, M.I.T., 1978).

14. K. Ikeuchi and B. K. P. Horn, Numerical shape from shading and occluding boundaries, *Artificial Intelligence*, **17**, 141-184, (1981).
15. A. R. Bruss, The Image Irradiance Equation: Its Solution and Application, Artificial Intelligence Laboratory, Technical Report TR-623 (Artificial Intelligence Laboratory, M.I.T., June 1981).
16. B. K. P. Horn, R. J. Woodham, and W. M. Silver, Determining Shape and Reflectance Using Multiple Images, AIM-490 (Artificial Intelligence Laboratory, M.I.T., August 1978).
17. R. J. Woodham Photometric method for determining surface orientation from multiple images, *Opt. Eng.*, **19**, 139-144 (1980).
18. W. M. Silver, Determining Shape and Reflectance Using Multiple Images, S. M. Thesis, Dept. of Electrical Engineering and Computer Science, M.I.T. (1980).
19. B. K. P. Horn, Hill-shading and the reflectance map, *Proc. IEEE*, **69**, 14-47 (1981).
20. B. K. P. Horn and B. L. Bachman, Using synthetic images to register real images with surface models, *Comm. ACM*, **21**, 914-924 (1978).
21. R. J. Woodham, Using digital terrain data to model image formation in remote sensing, in *Proc. Society of Photo-Optical Instrumentation Engineers*, vol. 238, Image Processing for Missile Guidance (1980), pp. 361-369.
22. S. Chandrasekhar, *Radiative Transfer* (Dover, New York, 1960).
23. S. Ueno, H. Kagiwada, and R. Kalaba, Radiative transfer in spherical shell atmospheres with radial symmetry, *J. Math. Phys.*, **12**, 1279-1286 (1971).
24. G. I. Marchuk *et al.*, *The Monte Carlo Methods in Atmospheric Optics* (Berlin, Springer-Verlag, 1980).
25. B. K. P. Horn and R. W. Sjöberg, Calculating the reflectance map, *Appl. Opt.*, **18**, 1770-1779 (1979).
26. F. E. Nicodemus, J. C. Richmond, J. J. Hsia, I. W. Ginsberg, and T. Limperis, Geometrical Considerations and Nomenclature for Reflectance, Monograph 160 (National Bureau of Standards, Washington, DC, 1977).
27. R. E. Turner, Radiative Transfer in Real Atmospheres, Technical Report ERIM 190100-24-T (Environmental Research Institute of Michigan, Ann Arbor, MI, 1974).
28. J. A. Smith, T. L. Lin, and K. J. Ranson, The Lambertian assumption and Landsat data, *Photo. Eng. Rem. Sens.*, **46**, 1183-1189 (1980).
29. B. Brennan and W. R. Bandeen, Anisotropic reflectance characteristics of natural earth surfaces, *Appl. Opt.*, **9**, 405-412 (1970).
30. R. E. Turner and M. M. Spencer, Atmospheric model for correction of spacecraft data, *Proc. 8th International Symp. on Remote Sensing of Environment* (Ann Arbor, 1972), pp. 895-934.

31. J. Otterman, Single-scattering solution for radiative transfer through a turbid atmosphere, *Appl. Opt.*, **17**, 3431-3438 (1978).
32. P. Moon, Illumination from a non-uniform sky, *Illumination Engineering*, **XXXVII**, 707-726 (1942).
33. B. K. P. Horn and R. J. Woodham, Destriping Landsat MSS images by histogram modification, *Computer Graphics and Image Processing*, **10**, 69-83 (1979).
34. S. L. Valley, *Handbook of Geophysics and Space Environments* (McGraw-Hill, New York, 1965).
35. I. Elterman, *UV, Visible, and IR Attenuation for Altitudes to 50 km, 1968*, Optical Physics Lab., project 7670, AFCRL-68-0153, Environmental Research Papers, no. 285 (Air Force Cambridge Research Labs., 1968).
36. R. J. Woodham, Looking in the shadows, Working Paper 169 (Artificial Intelligence Laboratory, M.I.T., 1978).
37. A. K. Mackworth, Interpreting pictures of polyhedral scenes, *Artificial Intelligence*, **4**, 121-137 (1973).
38. *Landsat Data Users Handbook*, revised edition. Available from Branch of Distribution, U.S. Geological Survey, Arlington, VA 22202 (1979).
39. J. Otterman and R. S. Fraser, Earth-atmosphere system and surface reflectivities in arid regions from Landsat MSS data, *Rem. Sens. of Environ.*, **5**, 247-266 (1976).
40. R. J. Woodham, Two simple algorithms for displaying orthographic projections of surfaces, Working Paper 126 (Artificial Intelligence Laboratory, M.I.T., 1976).
41. D. G. Luenberger, *Introduction to Linear and Nonlinear Programming* (Addison-Wesley, Reading, 1973).
42. R. A. McClatchey, R. W. Fenn, J. E. Selby, F. E. Volz, and J. S. Garing, Optical properties of the atmosphere, section 14 of *Handbook of Optics* (Optical Society of America, 1978).
43. K. L. Coulson, J. V. Dave, and Z. Sekera, *Tables Related to Radiation Emerging from a Planetary Atmosphere with Rayleigh Scattering*, (University of California Press, Berkeley, 1960).
44. K. Coulson, Effect of surface reflection on the angular and spectral distribution of skylight, *J. Atmos. Sci.*, **25**, 759-770 (1968).
45. M. P. Thekaekara, Proposed standard values of the solar constant and the solar spectrum, *J. Environ. Sci.*, **13**, 6-9 (1970).
46. R. H. Rogers, Investigation of Techniques for Correcting ERTS Data for Solar and Atmospheric Effects, Interim Report, NASA-CR-132860 (1973).
47. F. J. Ahern, P. M. Teillet, and D. G. Goodenough, Transformation of atmospheric and solar illumination conditions on the CCRS image analysis

- system, in *Proc 5th Symp. Machine Processing of Remotely Sensed Data*, (Laboratory for Applications of Remote Sensing, Purdue University, West Lafayette, IN, 27-29 June, 1979), pp. 34-52.
48. F. J. Ahern, D. G. Goodenough, S. C. Jain, and V. R. Rao, Use of clear lakes as standard reflectors for atmospheric measurements, in *Proc. 11th International Symp. on Remote Sensing of Environment* (Ann Arbor, 25-29 Apr., 1977), pp. 731-755.
 49. K. R. Piech and J. R. Schott, Atmospheric corrections for satellite water quality studies, in *Proc. Society of Photo-Optical Instrumentation Engineers*, **51**, 84-89 (1974).
 50. D. W. Starr and A. K. Mackworth, Exploiting spectral, spatial and semantic constraints in the segmentation of Landsat images, *Canadian J. of Rem. Sens.*, **4**, 101-107 (1978).

Table 1.

Orbital and multispectral scanner parameters for Landsat 1 (ERTS 1).

Orbital Parameters (from [38])

Launch date	23 July 1972
Nominal altitude	919 km
Semi-major axis	7285.438 km
Inclination	99.906°
Period	103.143 min
Eccentricity	0.001070
Time of descending node (time of equatorial crossing)	8:50 a.m.
Coverage duration	18 days
Revolutions per orbit	251
Distance between adjacent ground tracks at equator	159.38 km

Imaging System (from [38])

Scan lines (along track)	2340
Pixels per line (cross-track)	3000-3450
Nominal image size	185.3 km, square
Cross-track overlap at equator	14%
Cross-track overlap at 80° N,S	85%
Crosstrack field of view	11.56°
Nadir-point velocity	6.456 km/sec
Instantaneous field of view (IFOV)	0.086 × 0.086 mrad
Nominal IFOV at 919 m altitude, nadir direction	79 m
Effective IFOV, cross-track (less cross-track overlap)	56 m

Multispectral Scanner Sensitivities (from [39])
(mW cm⁻²sr⁻¹)

Band	Spectral Interval (nm)	Low	High
4	500-600 (green-yellow)	0.00	2.48
5	600-700 (orange-red)	0.00	2.00
6	700-800 (red-infrared)	0.00	1.76
7	800-1100 (infrared)	0.00	4.60

Table 2.

Theoretical path radiance L_p values by optical depth. For the computational values below, the solar zenith angle θ_0 is such that $\cos \theta_0 = 0.6$. Mean surface albedo is given by $\bar{\rho}$. Values are in $\text{mW cm}^{-2}\text{sr}^{-1}$.

Source	$\bar{\rho}$	Optical Depth, τ_0					
		0.02	0.05	0.10	0.15	0.25	0.50
(1)	0.0	0.0289	0.0734	0.1468	0.2186	0.3567	0.6642
(1)	0.25	0.0546	0.1342	0.2584	0.3720	0.5728	0.9534
(2)	0.1	0.0306	0.0754	0.1470	0.2149	0.3408	0.6068
(2)	0.2	0.03376	0.0830	0.1616	0.2361	0.3737	0.6615
(3)	0.1	0.01831	0.04420	0.08367	0.1192	0.1804	0.2904

Sources:

- (1) Numerical solution to the radiative transfer problem by Coulson, Dave, and Sekera [43].
- (2) Turner and Spencer two-stream approximation [30]. Their forward-scattering coefficient $\eta = 0.793$, and optical depth (both Rayleigh and aerosol components) are from the U.S. Standard Atmosphere.
- (3) Otterman's single-scattering approximation [31]. His forward-scattering fraction $f = 0.75$. Both Rayleigh and aerosol components are assumed.

Table 3.

Theoretical sky irradiance on a horizontal surface. The solar zenith angle θ_0 is such that $\cos \theta_0 = 0.6$. Mean surface albedo is given by $\bar{\rho}$. Values are in mW cm^{-2} .

Source	$\bar{\rho}$	Optical Depth, τ_0					
		0.02	0.05	0.10	0.15	0.25	0.50
(1)	0.0	0.1744	0.4241	0.8100	1.165	1.776	2.848
(1)	0.25	0.2248	0.5407	1.020	1.454	2.189	3.444
(2)	0.1	0.2933	0.4706	0.8966	1.280	1.940	3.081
(2)	0.2	0.2133	0.5173	0.9812	1.397	2.107	3.324
(3)	0.1	0.2832	0.6868	1.306	1.865	2.819	4.461
(3)	0.2	0.2913	0.7067	1.345	1.921	2.907	4.613
(4)	0.1	0.2703	0.6570	1.256	1.803	2.759	4.516

Sources:

- (1) Numerical solution to the radiative transfer problem by Coulson, Dave, and Sekera [43]. The author obtained sky irradiance values by numerically integrating the published sky radiances.
- (2) Extension due to Coulson [44] of (1) above, in which multiple reflection at the atmosphere/background interface is included in sky irradiance.
- (3) Turner and Spencer two-stream approximation [30]. Their forward-scattering coefficient $\eta = 0.793$, and optical depth (both Rayleigh and aerosol components) are from the U.S. Standard Atmosphere.
- (4) Otterman's single-scattering approximation [31]. His forward-scattering fraction $f = 0.75$. Both Rayleigh and aerosol components are assumed.

Table 4.

Measured atmospheric radiometric quantities. The values for most of the radiometric quantities are averages over the relevant spectral band, or the value at the center of the band for those items which vary slowly with wavelength.

Reference	Quantity	Band 4	Band 5	Band 6	Band 7
[34]	E_0	19.3	16.3	12.8	24.8
[45]	E_0	17.7	15.15	12.37	24.88
[46]	E_0	18.65	15.11	12.33	25.17
[34]	T_u	0.718	0.777	0.805	0.847
[46]	T_u	0.752	0.824	0.852	0.877
[47]	T_u	0.68	0.73	0.81	0.90
[34]	τ	0.331	0.252	0.217	0.166
[46]	τ	0.285	0.194	0.160	0.131
[47]	τ	0.386	0.315	0.211	0.105
[46]	L_p	0.268	0.127	0.081	0.103
[47]	L_p	0.286	0.164	0.153	0.185
[46]	E_s	1.9	1.25	0.9	1.46
[47]	E_s	4.00	3.12	2.03	2.29
[47]	$\bar{\rho}$	0.11	0.09	0.21	0.25

Notes:

- (i) Extraterrestrial solar irradiance E_0 is expressed in mW cm^{-2} .
- (ii) Sky irradiance E_s is in mW cm^{-2} over a horizontal surface.
- (iii) Path radiance L_p is expressed in $\text{mW cm}^{-2}\text{sr}^{-1}$.
- (iv) Rogers' data [46] was collected with a solar zenith angle of $\theta_0 = 48.0^\circ$.
- (v) The data from Ahern *et al.* [47] was collected with a solar zenith angle of $\theta_0 = 40.0^\circ$.

Table 5.

Model parameters used in models D1 through D12. Scale heights H , H_p , and H_s are in meters. Path radiance L_{p0} is in $\text{mW cm}^{-2}\text{sr}^{-1}$. Sky irradiance E_{s0} is in mW cm^{-2} .

Model	τ_0	H	L_{p0}	H_p	E_{s0}	H_s
D1	0.2	2529.4	0.315	4720.0	3.0	4720.0
D2	0.3	2529.4	0.315	4720.0	3.0	4720.0
D3	0.26185	1000.0	0.315	4720.0	3.0	4720.0
D4	0.26185	7000.0	0.315	4720.0	3.0	4720.0
D5	0.26185	2529.4	0.250	4720.0	3.0	4720.0
D6	0.26185	2529.4	0.376	4720.0	3.0	4720.0
D7	0.26185	2529.4	0.315	2000.0	3.0	4720.0
D8	0.26185	2529.4	0.315	9000.0	3.0	4720.0
D9	0.26185	2529.4	0.315	4720.0	2.0	4720.0
D10	0.26185	2529.4	0.315	4720.0	4.0	4720.0
D11	0.26185	2529.4	0.315	4720.0	3.0	2000.0
D12	0.26185	2529.4	0.315	4720.0	3.0	9000.0

Figure 1.

Global coordinate system relating the sun, satellite, and earth's surface. The y -axis points north, the x -axis east, and the z -axis upward. Directions are measured by pairs of polar and azimuthal angles, (θ, ϕ) . The sun is infinitely distant along (θ_0, ϕ_0) , and the satellite is infinitely distant along (θ_m, ϕ_m) . In the research discussed here, the satellite was directly over the imaged area, along the z -axis. The surface element or target (exaggerated in size here) is oriented so that its surface normal points along (θ_n, ϕ_n) . The origin is shown coincident with the target to illustrate the direction angles, although it normally would be conveniently located in, say, the southwest corner of the imaged area.

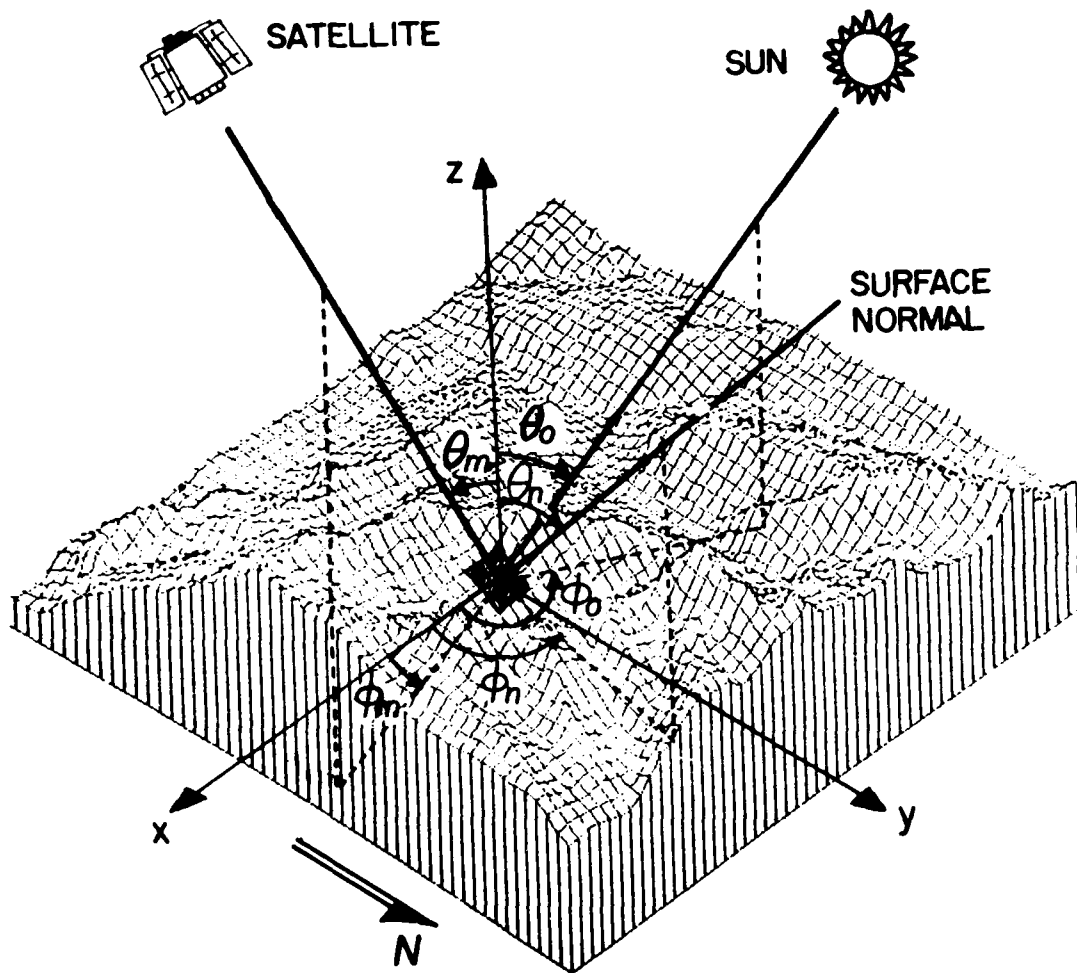


Figure 2.

In the local coordinate system, the axes are chosen with respect to the orientation of the target. The surface normal defines the z' -axis, making an angle θ_n with respect to the global z -axis. The x' -axis is chosen as the vertical projection of the global x -axis. In this local system, sun and satellite are infinitely distant in directions (θ'_0, ϕ'_0) and (θ'_m, ϕ'_m) respectively.

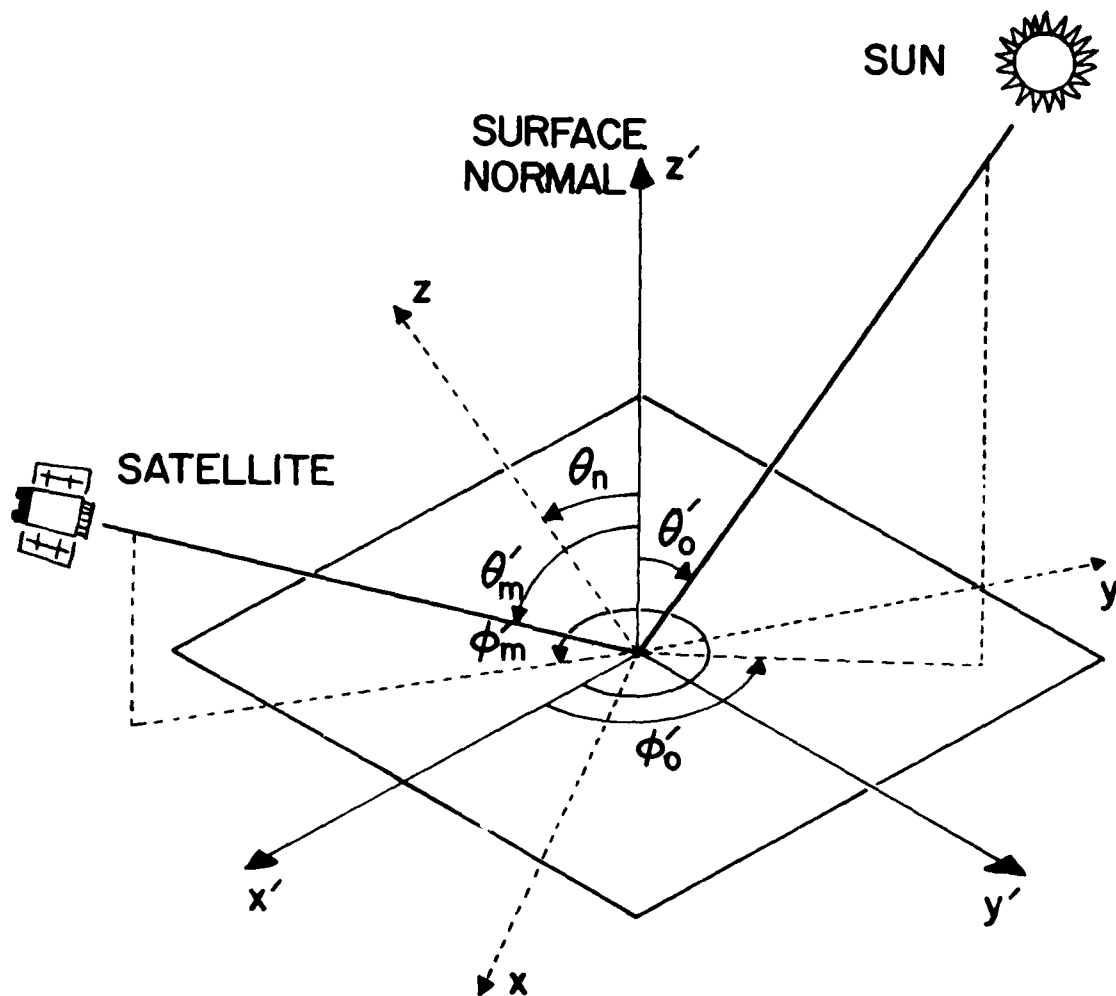


Figure 3.

Variation of optical depth and vertical transmission with altitude. The data is from the U.S. Standard Atmosphere for molecular and aerosol scattering components [34] for wavelengths between 500 and 600 nm. Vertical transmission is related to optical depth by $T_v(z) = e^{-\tau(z)}$.

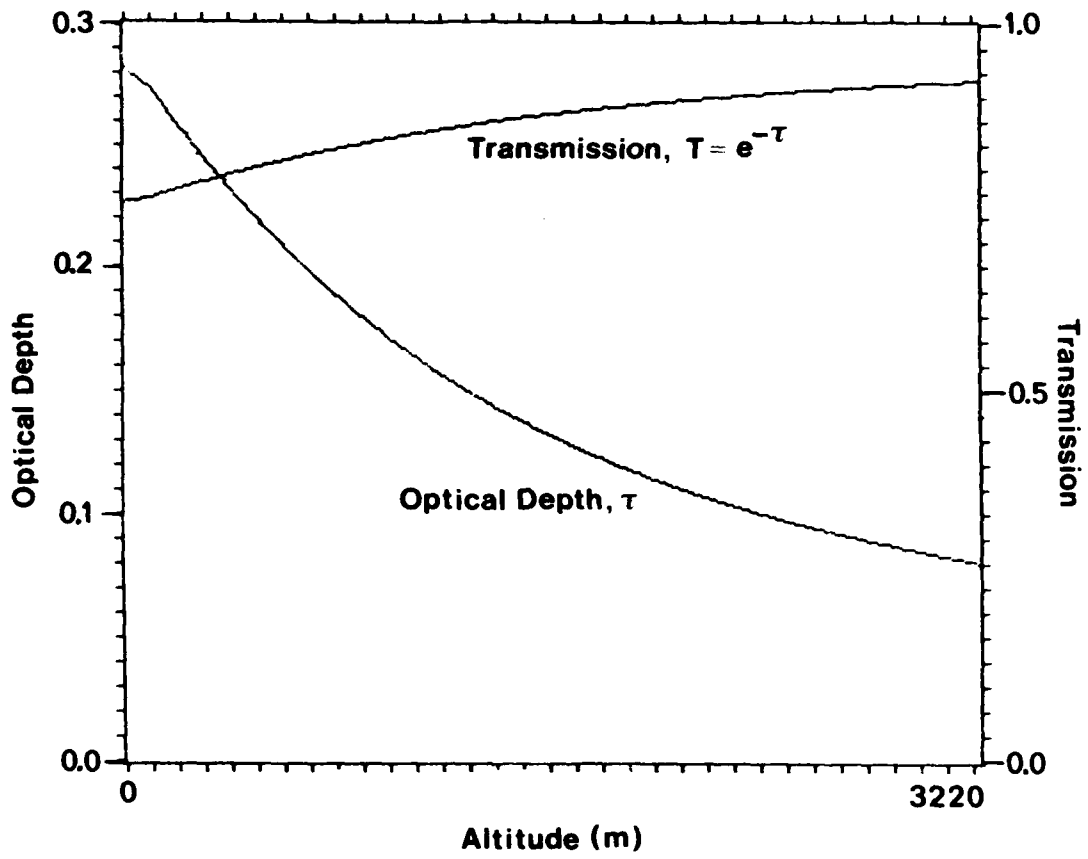


Figure 4.

Illustration of the atmospheric radiation components directly affecting remote imaging. The target is irradiated by attenuated sunlight, E_{sun} , reflection from surrounding terrain, L_g , and by the several components of diffuse skylight: primary scattering, L_{sp} , multiple scattering, L_{sm} , surface backscatter, L_{sb} , and cloud radiance, L_{sc} . The reflected target radiance L_t is attenuated in its travel to the satellite and contaminated by path radiance. The path radiance comes from primary scattering, L_{pp} , multiple scattering, L_{pm} , the background, L_{pb} , and (not shown) cloud radiance.

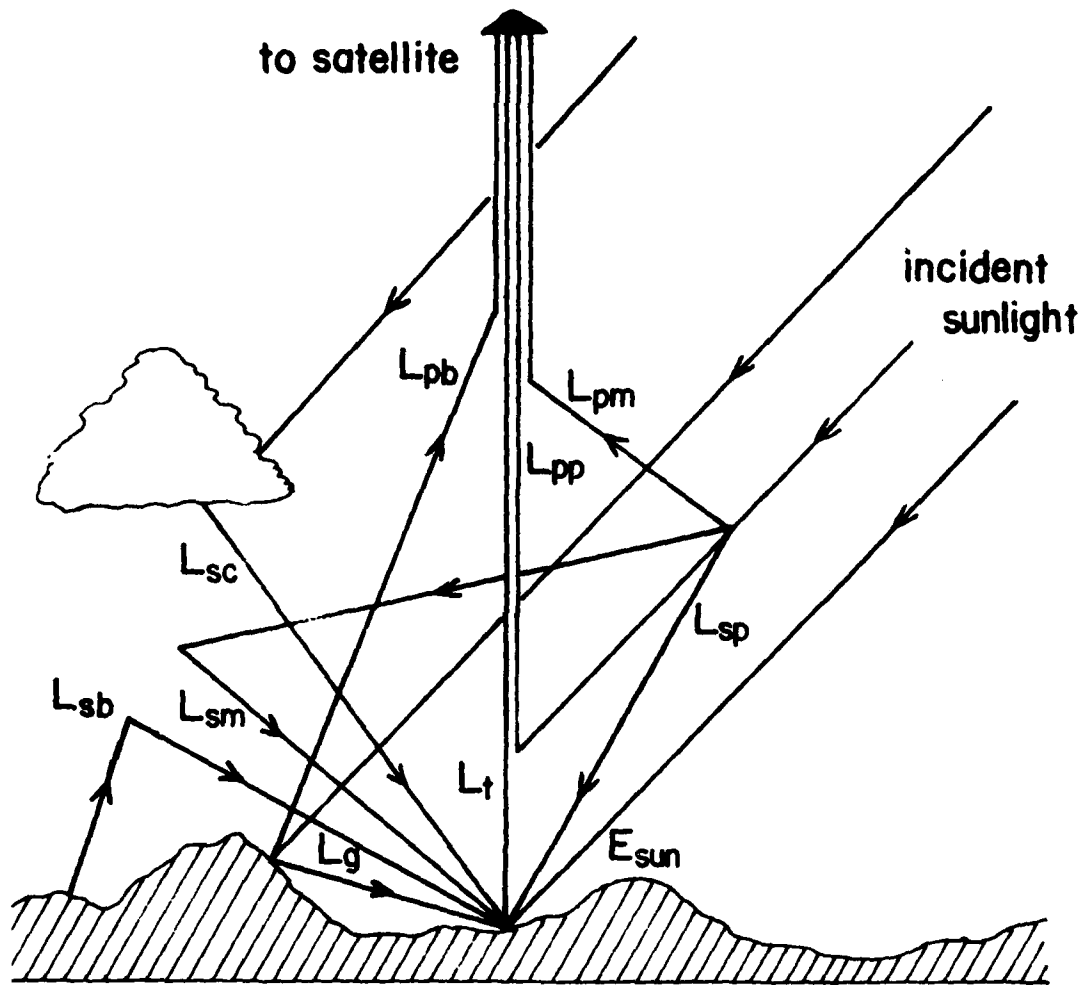


Figure 5.

Comparing path radiance as a function of altitude for the Turner-Spencer model [30] and the exponential approximation thereof. The calculation for the Turner-Spencer curve used a forward-scattering coefficient $\eta = 0.796$, average background albedo $\bar{\rho} = 0.15$, and a Rayleigh single-scattering phase function. The exponential curve, $L_p(z) = L_{p0}e^{-z/H_p}$, was fit by least squares to yield $L_{p0} = 0.376 \text{ mW cm}^{-2} \text{ sr}^{-1}$ and $H_p = 2732.56 \text{ m}$.

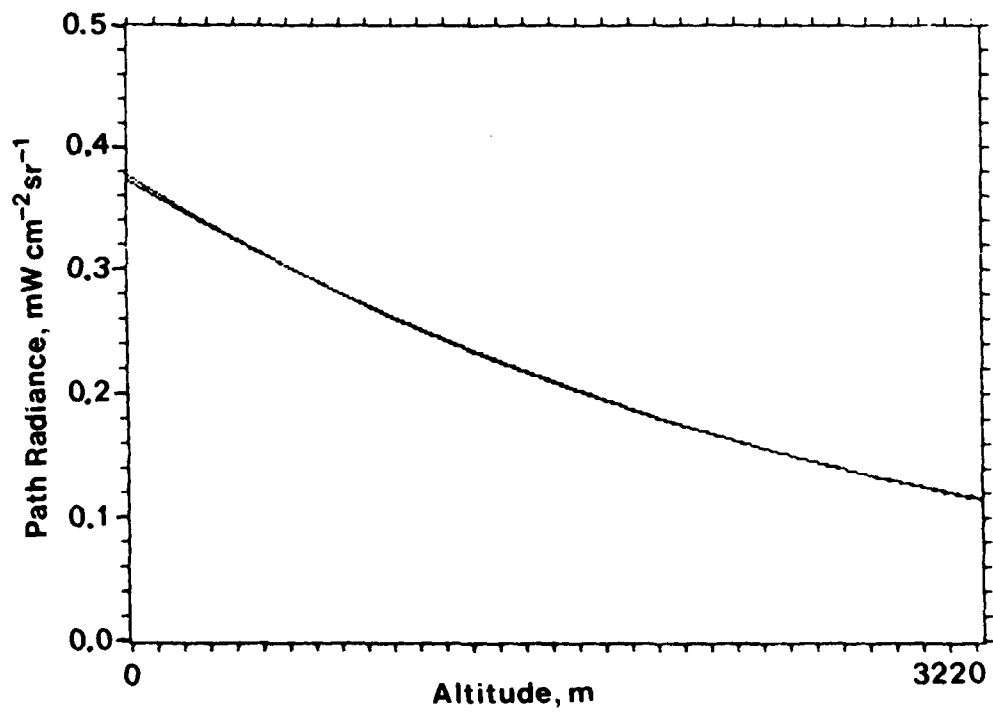


Figure 6.

Comparing sky irradiance on a horizontal surface as a function of altitude for the Turner-Spencer model [30] and the exponential approximation thereof. The calculation for the Turner-Spencer curve used a forward-scattering coefficient $\eta = 0.796$, average background albedo $\bar{p} = 0.15$, and a Rayleigh single-scattering phase function. The exponential curve, $E_s(z) = E_{s0}e^{-z/H_s}$, was fit by least squares to yield $E_{s0} = 3.04 \text{ mW cm}^{-2}$ and $H_s = 2944.9 \text{ m}$.

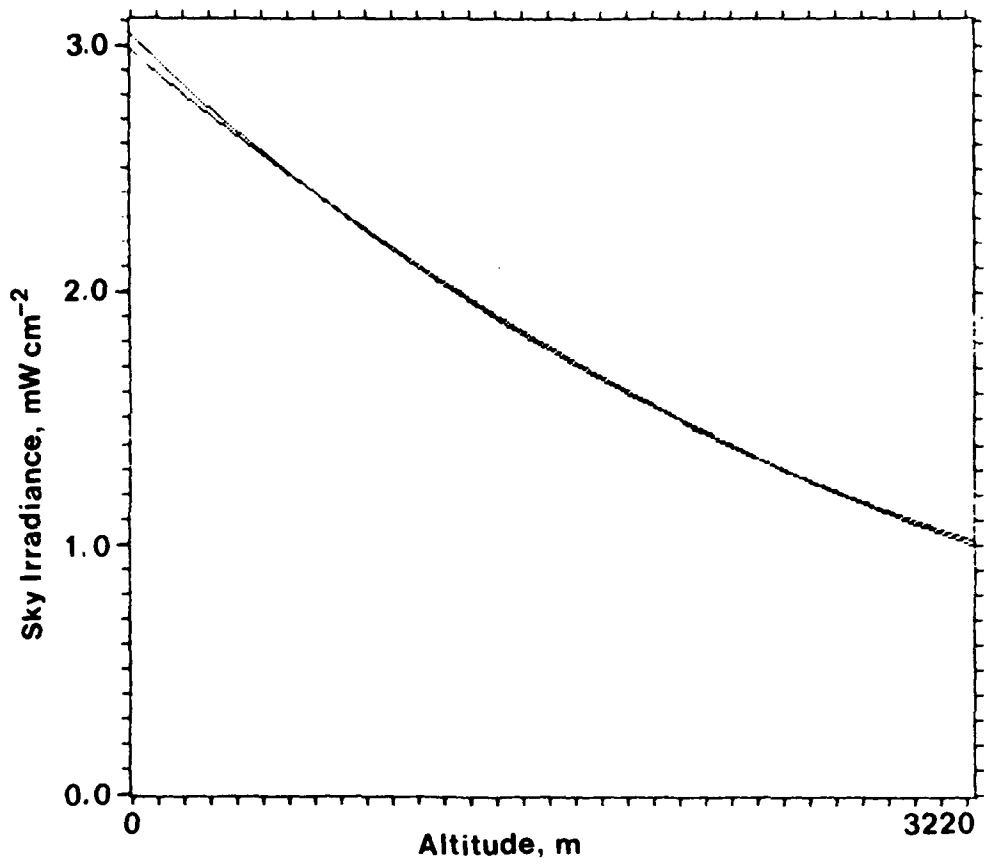


Figure 7.

An isometric plot of the Dent de Morcles region. The view is from the southeast at an elevation of 45° . This picture was made from the digital elevation model using the orthogonal projection technique of Woodham [40].

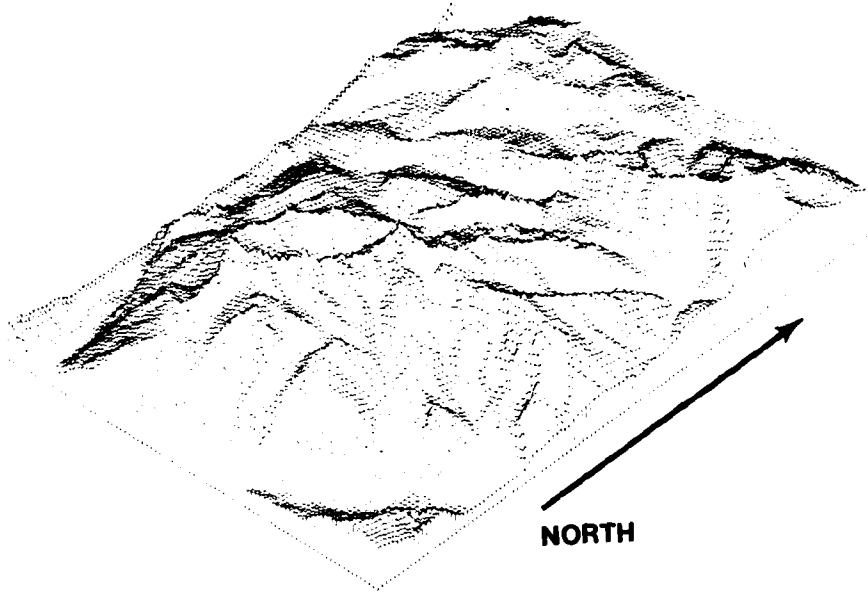


Figure 8.

The digital elevation model of the Dent de Morcles test region is displayed here as an image. Elevation is encoded as brightness, the brighter the area, the higher it is. The figure to the right is a histogram of elevation values, 0 meters on the far left, 5110 meters on the far right. The lowest point in the scene is 410 meters, the highest is 3210 meters. The peculiar disparity of adjacent altitudes in the histogram is an artifact of the process used to interpolate elevations during digitization of the contour maps (even altitudes were favored over odd ones). There are two histograms here: the smaller shaded one represents shadowed targets and the larger solid one sunlit targets (see the text).



Figure 9.

Landsat 1 multispectral scanner image for the yellow-green channel 4, 500-600 nm. The original raw image was destriped and rectified to be commensurate with the digital terrain models as described in the text. Note the presence of clouds in the upper left corner of the image and the pronounced hazy appearance due to atmospheric path radiance. The histogram records digitized image brightness. A value of 0 corresponds to a sensor radiance of $0.0 \text{ mW cm}^{-2} \text{ sr}^{-1}$. A value of 511 corresponds to a sensor radiance of $2.48 \text{ mW cm}^{-2} \text{ sr}^{-1}$. (As provided on computer compatible tape, Landsat MSS channels 4, 5, and 6 are represented by 7-bit bytes, channel 7 by 6-bit bytes. This data was scaled to 9-bit bytes during destriping and rectification, hence the maximum value of 511.) The peak at the high end of the histogram is due to saturation on clouds and snow.

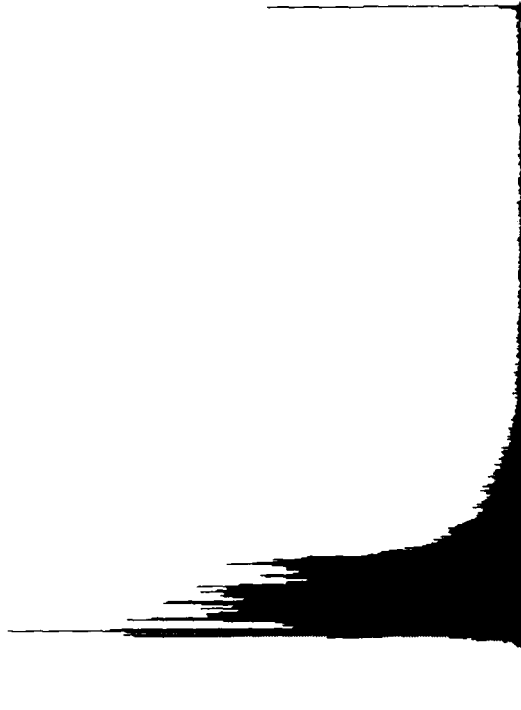
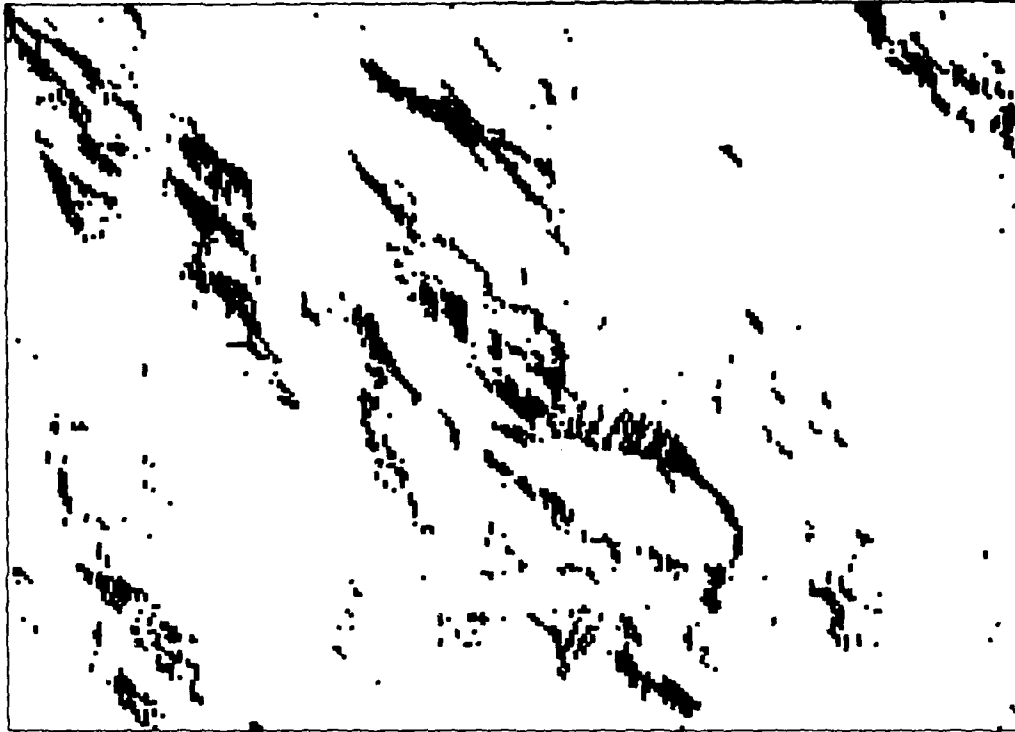
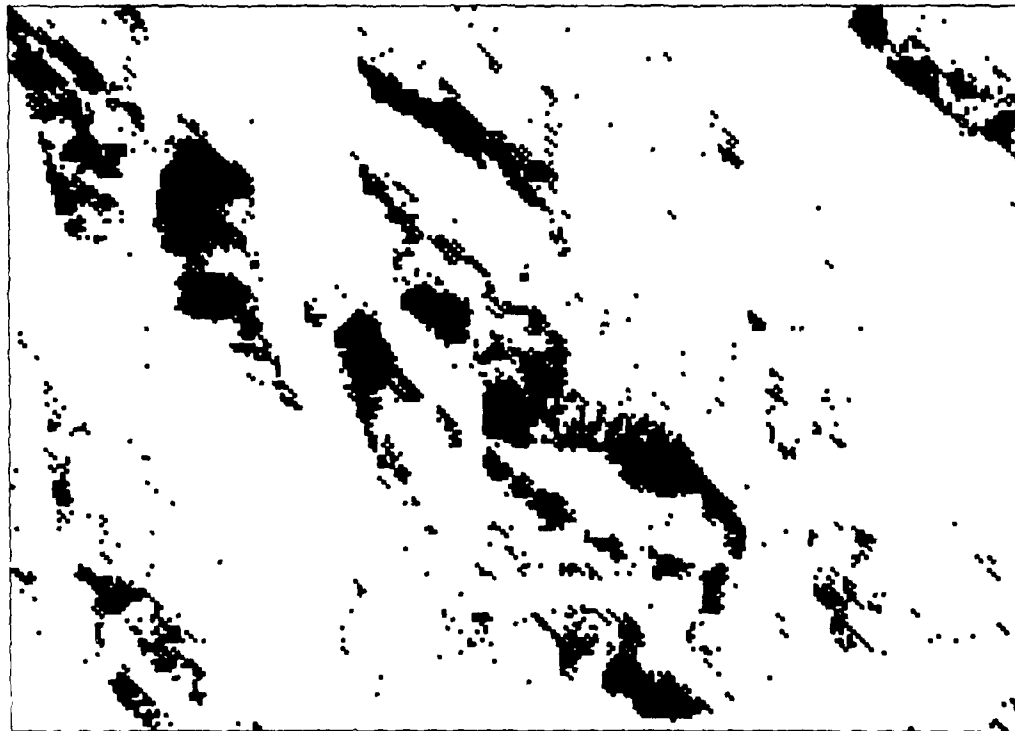


Figure 10.

The figure on the left is a binary map of those targets in the Dent de Morcles region that were in cast shadow under the illumination conditions of the Landsat overflight. The figure on the right is a binary map of those targets determined to lie in self-shadow (oriented away from the sun) under the given illumination. The shadow computation was performed using a method derived from hidden-surface plotting [40,21].



SELF-SHADOWS



CAST SHADOWS

Figure 11.

A synthetic image of the test region with the sun in the same position as during the Landsat overflight. The ground is assumed to be a Lambertian reflector of uniform albedo, $\rho = 1$. No atmosphere is assumed.

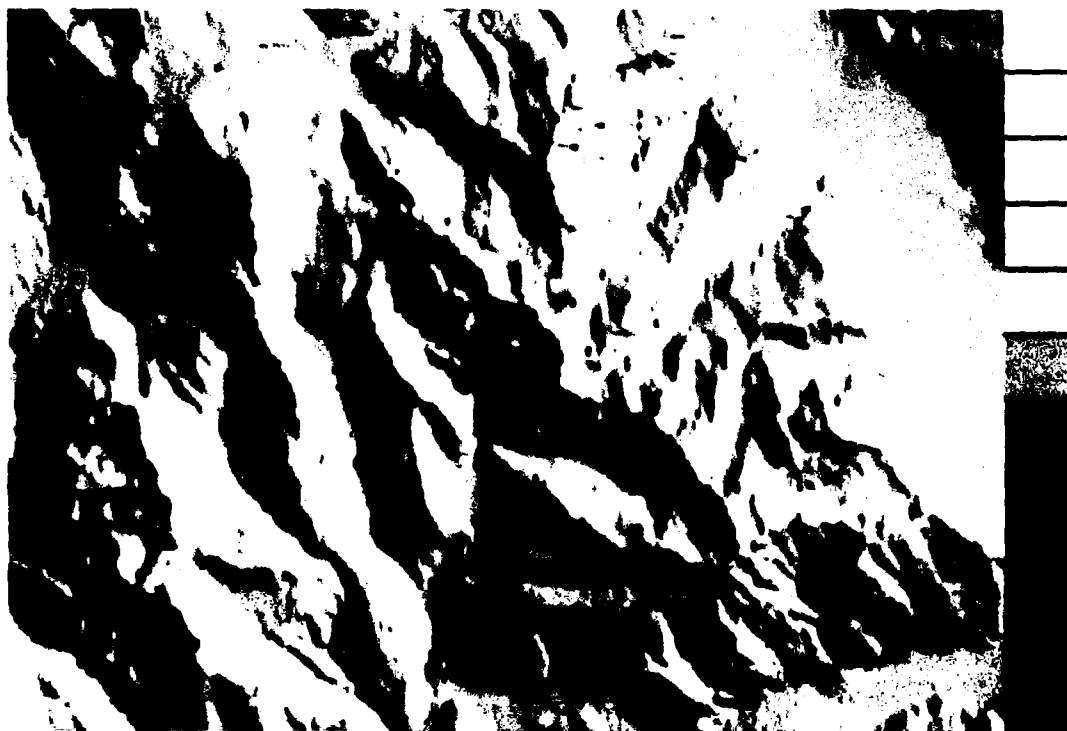
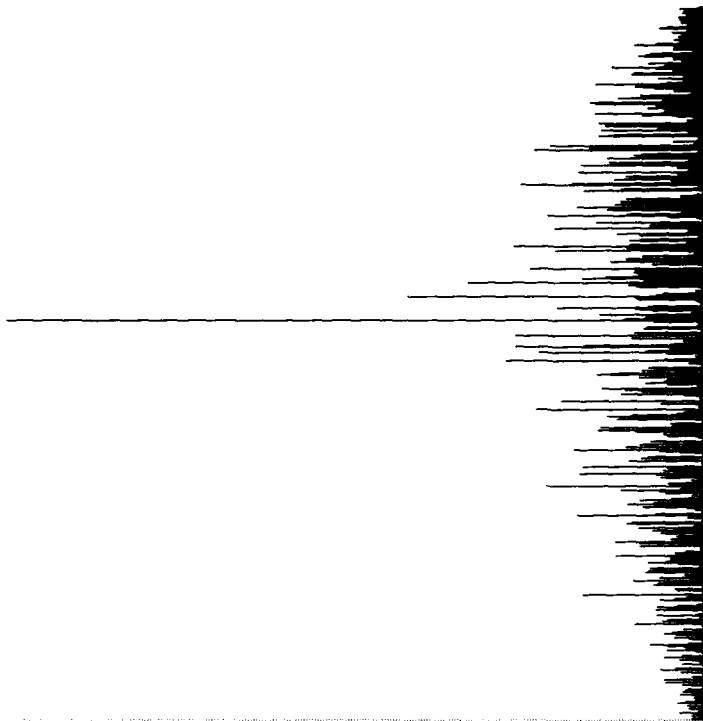


Figure 12.

Optical depth as a function of altitude for the U.S. Standard Atmosphere [34] for wavelengths in the band 500-600 nm. The three curves represent the Rayleigh or molecular scattering component, the aerosol scattering component, and the sum of the two. No ozone absorption is included in the total.

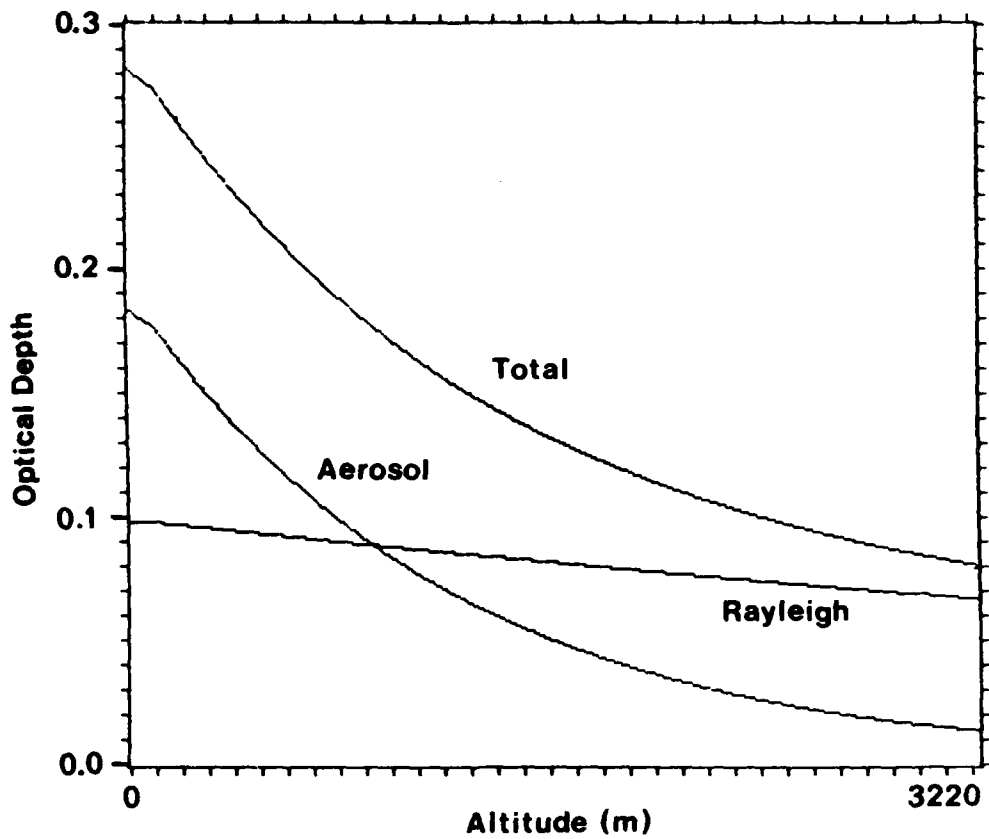


Figure 13.

Comparison of the two scattering components of the U.S. Standard Atmosphere and their total to approximate exponential functions derived from least-squares fitting. The approximate exponentials are superimposed on the curves from figure 12 . The parameters of the exponentials are given in the text.

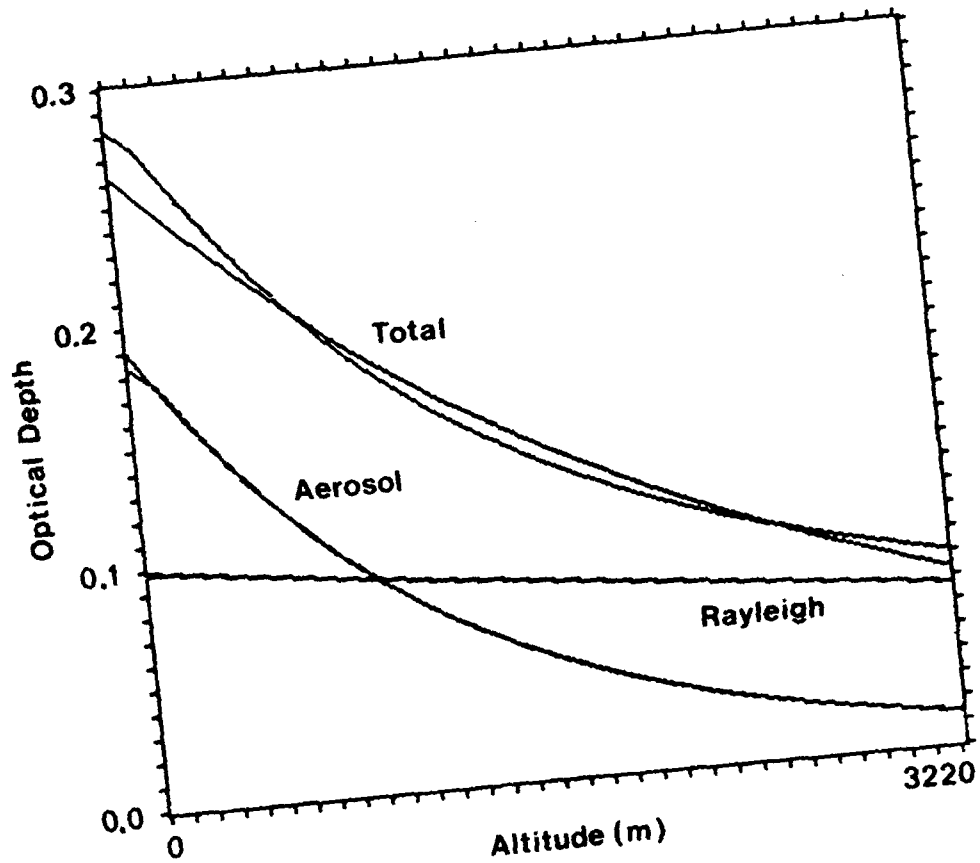


Figure 14.

Altitude profile of the minimum sensor radiance for Landsat multispectral scanner channel 4 (figure 9). Virtually all of these values originate in targets determined to lie in shadow during the satellite overflight.

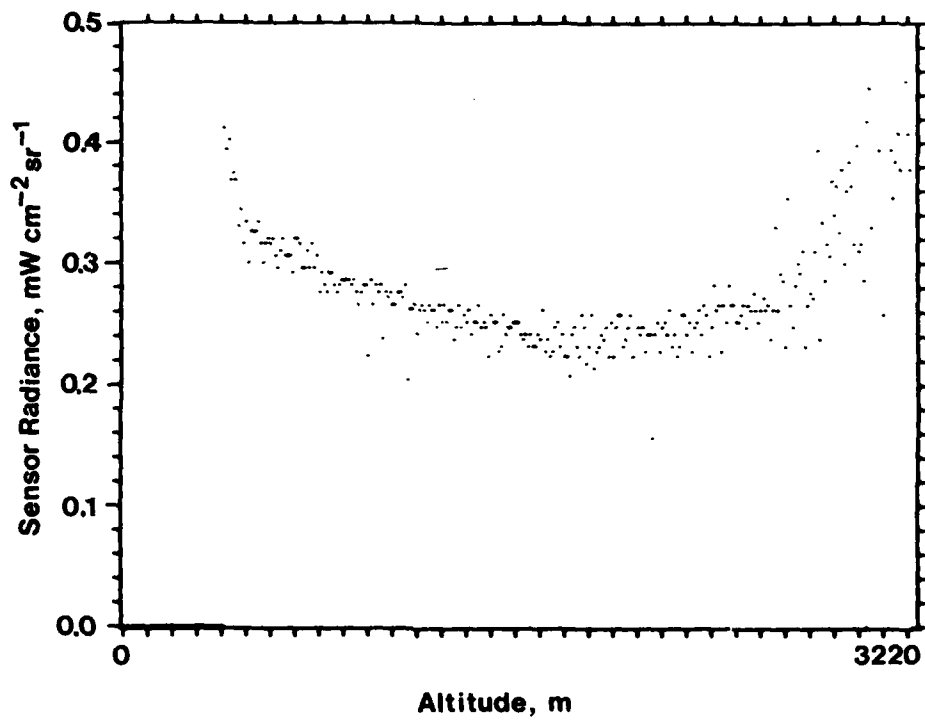


Figure 15.

Two possible exponential models of path radiance as inferred from minimum sensor data: $L_p(z) = L_{p0}e^{-z/H_p}$. For the upper curve, $L_{p0} = 0.33 \text{ mW cm}^{-2}\text{sr}^{-1}$; for the lower curve, $L_{p0} = 0.315 \text{ mW cm}^{-2}\text{sr}^{-1}$. $H_p = 4720 \text{ m}$ for both curves.

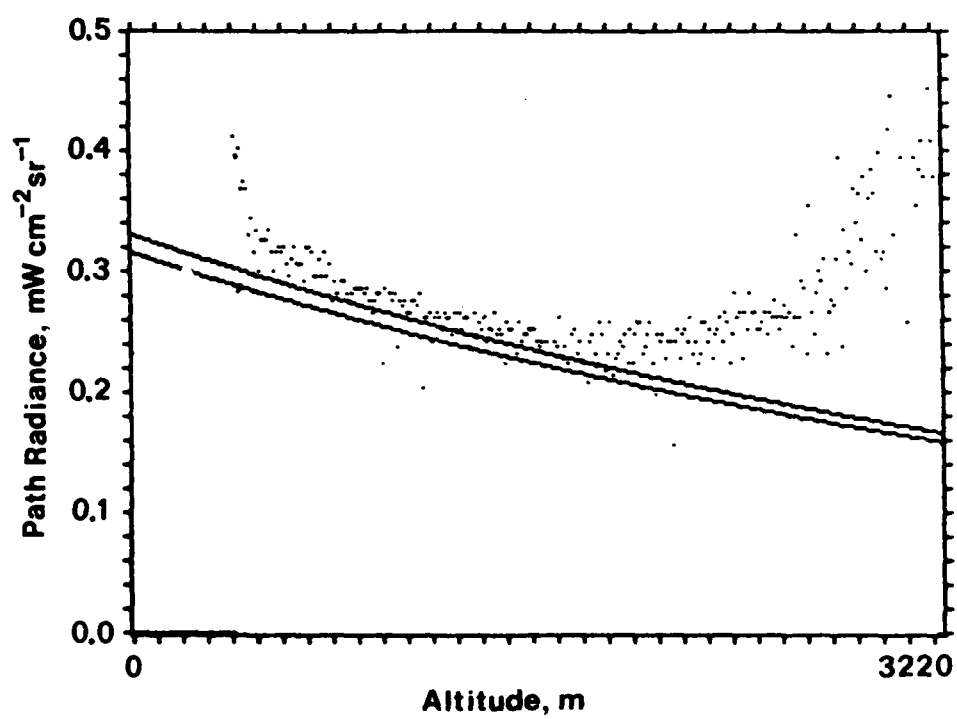


Figure 16.

Altitude profile of average albedo from sunlit targets in the Dent de Morcles test area. Albedo was calculated by assuming no intervening atmosphere and examining only sunlit targets at all altitudes. In such targets, reflected solar irradiance generally dominates, and computed albedo should approximate the true value. The data has been smoothed, but shows a distinct increase of albedo with altitude.

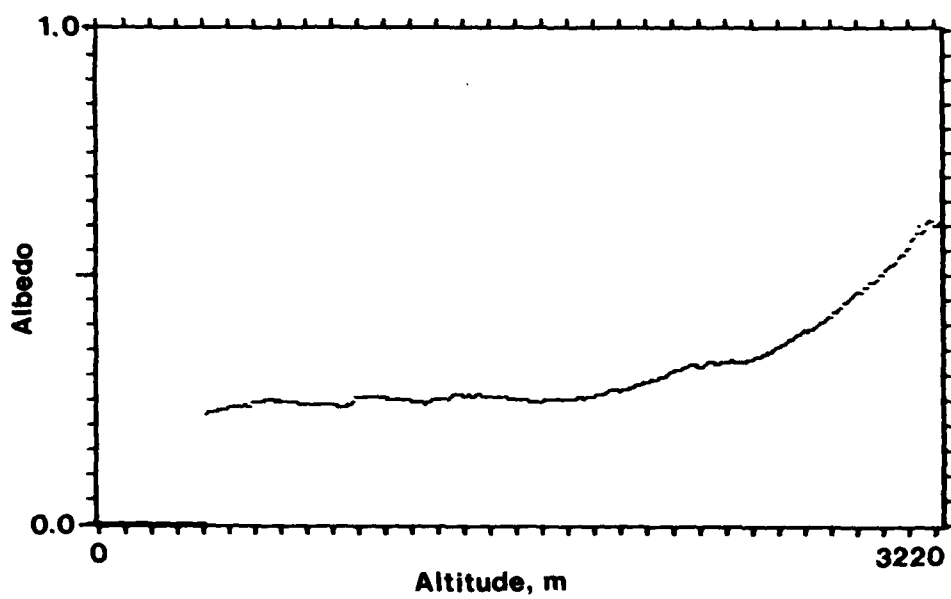


Figure 17.

Comparison of the exponential path radiance with a linear approximation. Parameters for the latter were derived by linearizing the exponential. Although a less steep line could be constructed that would better fit the data (and the exponential), the exponential is somewhat easier to handle and not significantly more costly to compute.

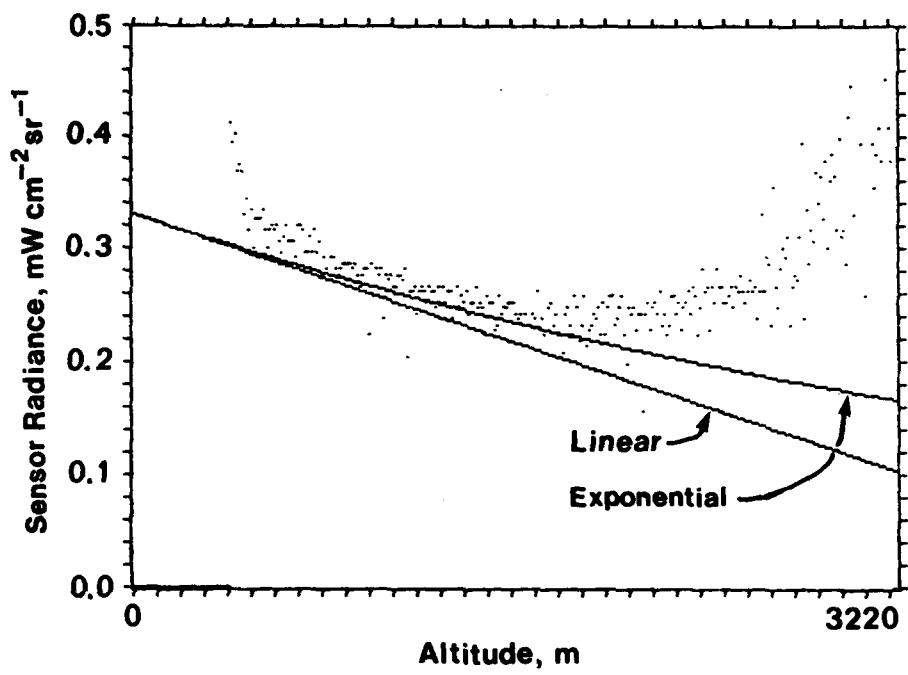


Figure 18.

Model A albedo image and its associated histogram. Albedo was computed using the following atmospheric model parameters:

$$\begin{array}{lll} \tau_0 = 0.26185 & L_{p0} = 0.376 \text{ mW cm}^{-2}\text{sr}^{-1} & E_{s0} = 3.04 \text{ mW cm}^{-2} \\ H = 2529 \text{ m} & H_p = 2734 \text{ m} & H_s = 2945 \text{ m} \end{array}$$

The average computed albedo for sunlit targets was $\bar{\rho} = 0.117$ and for shadowed targets $\bar{\rho} = 0.276$. The left end of the histogram represents $\rho = 0.0$ and the right end $\rho = 1.0$.

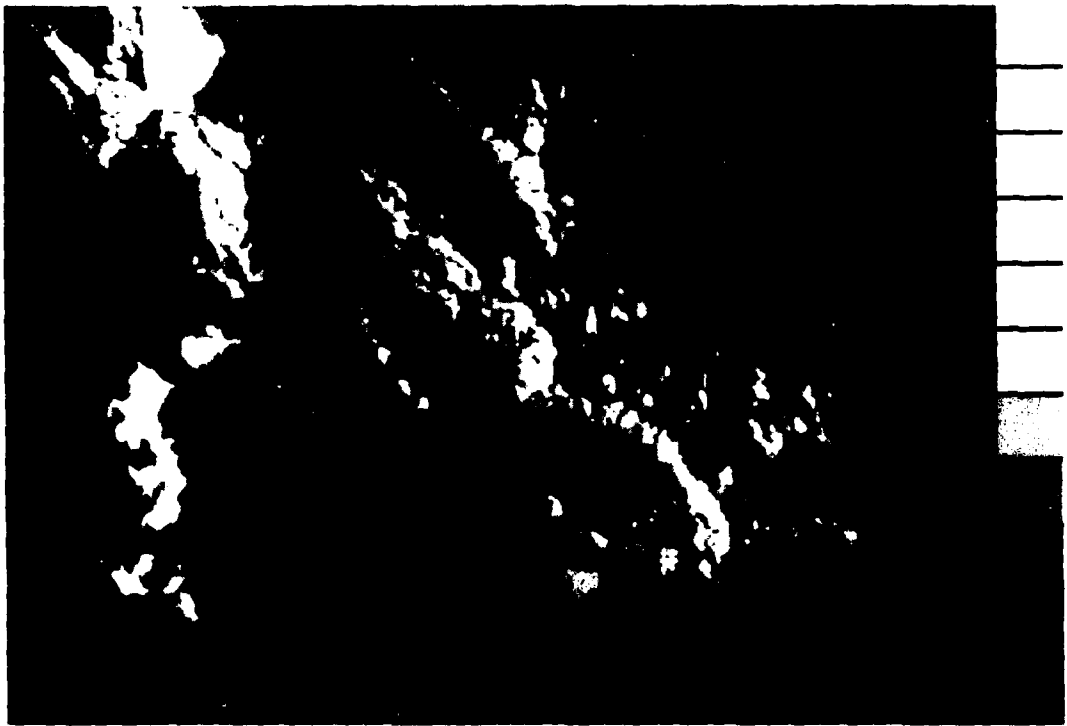
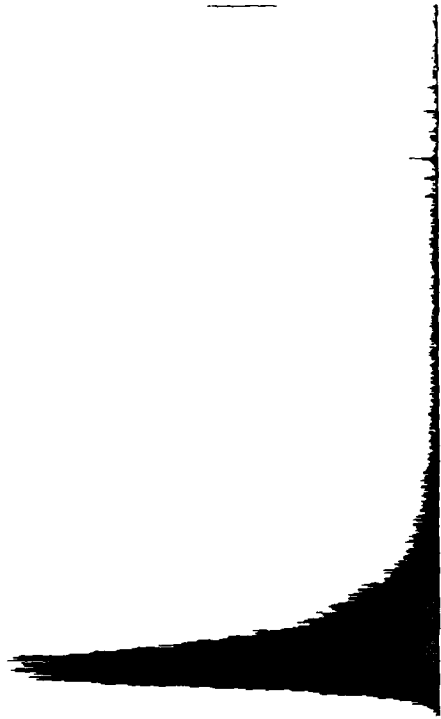


Figure 19.

Model B albedo image and its associated histogram. Albedo was computed using the following atmospheric model parameters:

$$\begin{array}{lll} \tau_0 = 0.26185 & L_{p0} = 0.315 \text{ mW cm}^{-2} \text{ sr}^{-1} & E_{s0} = 3.0 \text{ mW cm}^{-2} \\ H = 2529 \text{ m} & H_p = 4720 \text{ m} & H_s = 4720 \text{ m} \end{array}$$

The average computed albedo for sunlit targets was $\bar{\rho} = 0.110$ and for shadowed targets $\bar{\rho} = 0.200$. The left end of the histogram represents $\rho = 0.0$ and the right end $\rho = 1.0$.



Figure 20.

Model C albedo image and its associated histogram. Albedo was computed using the following atmospheric model parameters:

$$\begin{array}{lll} \tau_0 = 0.23 & L_{p0} = 0.33 \text{ mW cm}^{-2} \text{ sr}^{-1} & E_{s0} = 3.04 \text{ mW cm}^{-2} \\ H = 4000 \text{ m} & H_p = 2734 \text{ m} & H_s = 2945 \text{ m} \end{array}$$

The average computed albedo for sunlit targets was $\bar{\rho} = 0.108$ and for shadowed targets $\bar{\rho} = 0.184$. The left end of the histogram represents $\rho = 0.0$ and the right end $\rho = 1.0$.



Figure 21.

Illustration of the qualitative effects of changing the imaging model atmospheric parameters. The top left image is from model B. Images D1 through D6 are shown on this page left to right, top to bottom. Albedo image B is again shown on the next page, with images D7 through D12. Parameter values are listed in table 5.

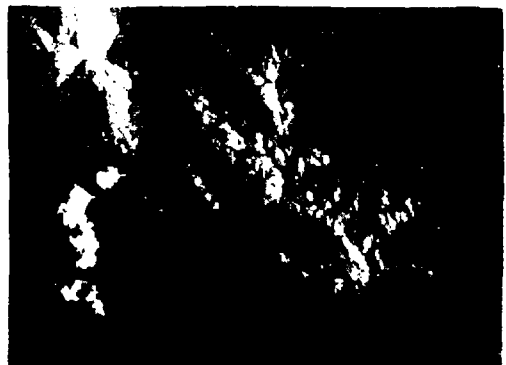
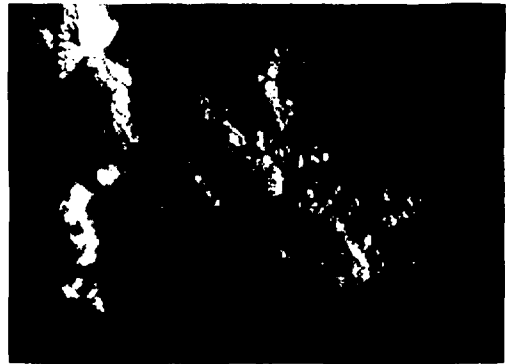
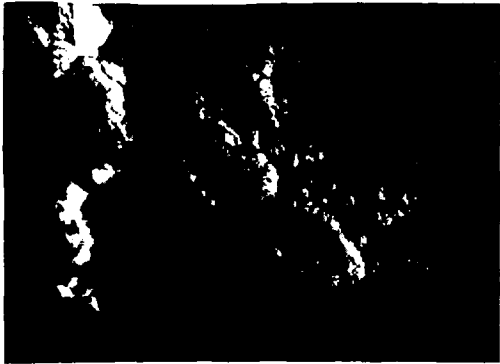


Figure 21(continued).

